Sensory neuropathy-causing mutations in ATL3 cause aberrant ER membrane tethering

Michiel Krols[1,2*], Sammy Detry[3,4,*], Bob Asselbergh[5,*], Leonardo Almeida-Souza[6], Anna Kremer[7,8], Saskia Lippens[7,8], Riet de Rycke[7,8,] Vicky De Winter[1,2], Franz-Josef Müller[9], Ingo Kurth[10], Harvey T. McMahon[6], Savvas N. Savvides[3,4], Vincent Timmerman[1,2,*] & Sophie Janssens[11,12,*]

[1]*Peripheral Neuropathy Research Group, Department of Biomedical Sciences, University of Antwerp, Antwerp, Belgium*

[2]*Institute Born Bunge, Antwerp, Belgium*

[3]*Unit for Structural Biology, VIB Center for Inflammation Research, Ghent University, Ghent, Belgium*

[4]*Laboratory for Protein Biochemistry and Biomolecular Engineering, Department of Biochemistry and Microbiology, Ghent University, Ghent Belgium*

[5]*VIB-UAntwerp Center for Molecular Neurology, University of Antwerp, Antwerp, Belgium*

[6]*MRC Laboratory of Molecular Biology, Cambridge, UK*

[7]*VIB BioImaging Core, VIB, Ghent, Belgium*

[8]*Department of Biomedical Molecular Biology, Ghent University, Ghent, Belgium*

[9]*Zentrum für Integrative Psychiatrie, University Hospital Schleswig-Holstein, Kiel, Germany*

[10]*Institute of Human Genetics, Medical Faculty, RWTH Aachen University, Aachen, Germany*

[11]*Unit Immunoregulation and Mucosal Immunology, VIB Center for Inflammation Research, Ghent University, Ghent, Belgium*

[12]*Department of Internal Medicine, Ghent University, Ghent, Belgium*

** These authors contributed equally*

Address of correspondence:
Prof. Dr. Sophie Janssens, PhD
Laboratory of Immunoregulation and Mucosal Immunology
VIB-UGhent, Center for Inflammation Research
Technologiepark 927
B-9052 Zwijnaarde
Belgium
Phone: +32-9-3313740
Fax: +32-9-2217673
Email: sophie.janssens@irc.vib-ugent.be

Prof. Dr. Vincent Timmerman, PhD
Peripheral Neuropathy Research Group
University of Antwerp - CDE
Parking P4, Building V, Room 1.30
Universiteitsplein 1

2610 Antwerpen
Belgium
Tel: +32-3-265.10.24
E-mail: vincent.timmerman@uantwerpen.be

ABSTRACT

The ER is a complex network of sheets and tubules that are continuously reshaped, fused and broken apart. The relevance of this remodeling process is underscored by the fact that mutations in atlastins (ATL), the proteins mediating ER fusion in mammalia, lead to neurodegenerative disease. While the mechanism of ATL-mediated membrane fusion has gained a lot of attention, how defects in this process lead to neurodegeneration is largely unknown. Here we show that the HSAN-causing ATL3 variants retain their dimerization-dependent GTPase activity, but are unable to form the stable crossover dimer necessary for membrane fusion. Instead they promote aberrant membrane tethering. This leads to a collapse of the ER network characterized by bundles of ER tubules running in parallel, as observed by volume electron microscopy and transmission electron microscopy in patient derived fibroblasts. Given the redundancy of the three ATL proteins in membrane fusion, this enhanced ER membrane tethering likely represents a major contribution to the axonal degeneration observed in patients.

INTRODUCTION

The endoplasmic reticulum (ER) is an intricate network of sheets and tubules that spreads throughout the cytoplasm and is continuous with the nuclear envelope. The distinct morphologies of the ER subdomains are determined by a tug of war between proteins promoting the high membrane curvature found in ER tubules and sheet edges on the one hand, and proteins segregating to and stabilizing ER sheets on the other. Adding to the complexity of this organelle, the network is continuously being remodeled through the extension and retraction of tubules, tubule fusions and ring closures (Westrate et al., 2015).

In metazoans, homotypic fusion of ER tubules is mediated by a class of membrane-bound dynamin-like GTPases known as Atlastins (ATLs) (Hu et al., 2009; Orso et al., 2009). The ATL proteins are comprised of a large N-terminal cytoplasmic domain, two closely spaced transmembrane helices that anchor the protein in the ER membrane, and a C-terminal amphipathic helix. The N-terminal domain consists of a GTPase domain (G domain) connected via a flexible linker to a three-helix bundle (3HB) middle domain (Bian et al., 2011; Byrnes and Sondermann, 2011; Liu et al., 2012). Homotypic ER membrane fusion is mediated by the GTP-dependent homodimerization of ATLs on opposing membranes, promoting tight membrane tethering and eventually membrane fusion (Byrnes and Sondermann, 2011; Byrnes et al., 2013; Hu and Rapoport, 2016; Liu et al., 2015; O'Donnell et al., 2017; Saini et al., 2014)(see Fig. S1). Although the actual fusion mechanism has not been entirely elucidated, it is clear that the ATL transmembrane domains and the C-terminal tail are crucial for membrane fusion, presumably by destabilizing the membranes to promote lipid mixing (Liu et al., 2012; Moss et al., 2011).

Mammals have three ATLs, which share high sequence homology but are differentially expressed. ATL1 is predominantly expressed in the brain, whereas ATL2 and ATL3 show a more ubiquitous expression pattern (Rismanchi et al., 2008). In addition, the three ATL proteins appear to have different fusogenic capacities, with ATL1 being the stronger fusogen and ATL3 a much weaker one (Hu et al., 2015; O'Donnell et al., 2017). In line with this, selective loss of ATL3 has very little effect on ER morphogenesis, whereas ATL1 alone is sufficient to rescue the loss of both ATL2 and ATL3 in COS-7 cells (Hu et al., 2015).

Mutations in ATL1 have been identified in patients suffering from degeneration of upper motor neurons (hereditary spastic paraplegia, HSP) as well as peripheral sensory neurons

(hereditary sensory and autonomic neuropathy, HSAN) (Guelly et al., 2011; Zhao et al., 2001). More recently two autosomal dominant missense-mutations in ATL3 were found to cause sensory neurodegeneration: p.Tyr192Cys and p.Pro338Arg, hereafter referred to as $ATL3^{Y192C}$ and $ATL3^{P338R}$ (Fischer et al., 2014; Kornak et al., 2014). HSP patients show progressive spasticity in the lower limbs whereas individuals affected by HSAN have a characteristic loss of pain perception and variable degrees of autonomic dysfunction. Common to both diseases is a degeneration of neurons with particularly long axons. Interestingly, mutations in additional ER shaping proteins such as REEP1, REEP2, Spastin, and Reticulon 2 cause similar phenotypes (Hübner and Kurth, 2014), clearly showing that maintaining the dynamic structure of the ER throughout these very long axons is pivotal for neuronal survival. What is less clear, however, is how defects in ER shaping underlie axonal degeneration. We therefore investigated whether disease-causing mutations in ATL3 alter its functionality and how this affects ER shaping and dynamics. Here, we reveal for the very first time evidence for aberrant ER membrane tethering caused by ATL3 mutations. Using volume electron microscopy, we provide unprecedented insights in the structure of the ER tangles resulting from this excessive tethering in cells expressing mutant ATL3. This phenotype is prominent in patient derived fibroblasts as well, excluding an artefact due to overexpression of mutant ATL3. Given the redundancy of the three atlastin proteins, the aberrant ER membrane tethering likely represents a major contribution to the axonal degeneration observed in patients.

RESULTS

Mutations in ATL3 disrupt ER morphogenesis

We recently uncovered two novel mutations in ATL3 to be causative for HSAN and with this finding added ATL3 to a growing list of ER shaping proteins involved in neurodegeneration (Fischer et al., 2014; Kornak et al., 2014). To study the impact of the ATL3 Y192C and P338R mutations on ER morphology, we imaged COS-7 cells co-expressing mRuby-KDEL as a luminal ER marker (Kredel et al., 2009) and GFP-tagged wild-type (WT) and mutant versions of ATL3 (Fig. S2). $ATL3^{WT}$ was targeted to the ER where it was present mostly in the highly curved membranes of ER tubules (Fig. 1A). $ATL3^{Y192C}$ or $ATL3^{P338R}$ similarly localized to the tubular ER (Fig. 1A). However, while $ATL3^{WT}$ spread evenly throughout the ER network, mutant ATL3 appeared in patches along the tubules in the peripheral ER and was present mostly in an ER region near the nucleus (Fig. 1A). Similar phenotypes were observed in HeLa cells (data not shown). The peripheral ER network morphology was dramatically altered in cells expressing mutant ATL3. While the ER in control cells formed a highly interconnected tubular network in the periphery of the cell (Fig. 1B), cells transfected with $ATL3^{Y192C}$ or $ATL3^{P338R}$ displayed a peripheral ER network that was far more disperse (Fig. 1B), as quantified by the significant decrease in density of threeway junctions per cell area (Fig. 1B,C). Concordantly, expression of either mutant ATL3 resulted in larger zones within the cell periphery that were devoid of ER tubules, defined as ER sparsity (Fig. 1B,D).

Besides ER morphogenesis, several reports have suggested a role for ATLs in the Golgi apparatus (Namekawa et al., 2007; Rismanchi et al., 2008). Neither WT nor mutant ATL3 were found to localize to the Golgi complex of HeLa or COS-7 cells, and overexpression of mutant ATL3 was not found to alter Golgi apparatus morphology in these cells (Fig. S3), indicating that a disruption of the ER tubular network is the main hallmark of these mutations in ATL3.

ER continuity is maintained in ATL3 mutant cells

A key feature of the ER is that despite the continuous membrane rearrangements, it maintains a single continuous lumen. In a recently reported *in vitro* reconstitution model of the ER, blocking ATL-mediated fusion resulted in fast fragmentation of the network (Powers et al., 2017). Given the severe effect of the mutations in ATL3 on ER morphology, we examined whether ER continuity was maintained in cells expressing mutant ATL3. Therefore, we co-expressed a photoactivatable GFP targeted to the ER lumen (PA-GFP-KDEL) (Jones et al., 2009)

in cells expressing mCherry-tagged ATL3. Photo-induced activation of this fluorescent protein allows tracking PA-GFP-KDEL as it pervades from the site of activation throughout the ER network, and thus allows assessing its luminal continuity (Video 1). In addition, the rate at which the fluorophores spreads throughout the ER can be used as a measure of network connectivity (Fig. S4). In cells expressing $ATL3^{WT}$, the activated PA-GFP rapidly diffuses from its site of activation throughout the ER network (Fig. 2A). Photo-activation in similar regions of the ER in mutant ATL3 expressing cells comparably resulted in the spread of the activated fluorophores throughout the entire network, indicating that luminal continuity is not disrupted in these cells (Fig. 2A). However, in agreement with a loss of threeway junctions, analysis of the rate at which the fluorescence intensity increased at discrete distances from the site of activation shows a significantly slower emergence of activated PA-GFP in distal regions of cells expressing $ATL3^{Y192C}$ or $ATL3^{P338R}$ compared to cells expressing $ATL3^{WT}$ (Fig. 2B and Fig. S4). This slowed diffusion through the ER network confirms that cells expressing mutant ATL3 fail to establish an intricately connected ER network (Fig. 1). Combined, these findings show that mutations in ATL3 affect the formation of threeway junctions without causing network fragmentation.

Reduced efficiency of ER membrane fusion in ATL3 mutant cells

Threeway junctions represent the nodes that interconnect the tubular ER and are established through homotypic ER membrane fusion. The loss of junctions in ATL3 mutant cells suggests that mutations in ATL3 disrupt ER membrane fusion. Therefore, live cell imaging of COS-7 cells expressing ATL3-GFP and mRuby-KDEL as an ER marker was performed to monitor events in which a newly forming tubule extends from an existing one and makes contact with an opposing tubule (Fig. 3A). When this contact resulted in a novel junction, it was scored as a successful ER membrane fusion event (Fig. 3A, Video 2). In contrast, when this interaction failed to establish a threeway junction and resulted in retraction of the extending tubule, it was considered a failed fusion event (Fig. 3A, Video 3). Compared to control cells, overexpression of $ATL3^{WT}$ significantly increased the ER membrane fusion success rate from 67 ± 2% to 78 ± 2% (Fig. 3B). Expression of mutant ATL3 on the other hand resulted in a dramatic reduction of this success rate to 23 ± 2% in the case of $ATL3^{Y192C}$ and 40 ± 2% in the case of $ATL3^{P338R}$ (Fig. 3B). Hence, the efficiency of ER membrane fusion is impaired

dramatically when ATL3 carrying the HSAN-causing mutations is expressed, indicating that the mutations cause a defect in the mechanism whereby ATL3 induces membrane fusion.

Mutations in ATL3 interfere with GTP hydrolysis-dependent dimerization

To probe the possible structural and mechanistic consequences of the Y192C and P338R mutations in the functional cycle of ATL3, we undertook structural analyses and comparative biochemical and biophysical studies employing the soluble domain of $ATL3^{WT}$, $ATL3^{Y192C}$ and $ATL3^{P338R}$ (encompassing the GTPase domain, the linker and the 3HB middle domain). Prior structural studies on ATL1 had revealed the existence of at least two distinct conformations of ATL1, termed “extended” and “crossover” (Fig. S1), which were hypothesized to correspond to the prefusion and postfusion states of ATL1, respectively (Bian et al., 2011; Byrnes and Sondermann, 2011). In the extended conformation, for which a crystal structure of ATL3 was also recently solved (O'Donnell et al., 2017), the alpha-helical 3HB middle domain packs tightly against the G domain, enforced mainly by hydrophobic interactions (Fig. 4A, S1). Interestingly, the Y192 and P338 residues in ATL3, affected in HSAN patients, localize to this hydrophobic core (Fig. 4A). At the same time, these amino acid residues pack against the hinge region that relays the drastic structural transitioning of ATL3 into its crossover conformation upon hydrolysis of GTP (Fig. 4A, B). It is thus clear that both mutations affect residues that are positioned within a functional switch region in ATL3 (Fig. 4A). The functional relevance of these residues is further underscored by the fact that mutations at the equivalent positions in the homologous ATL1 cause HSP (de Bot et al., 2013; McCorquodale et al., 2011).

To enable comparative biochemical and biophysical characterization of $ATL3^{WT}$, $ATL3^{Y192C}$, and $ATL3^{P338R}$ we produced and purified recombinant WT and mutant proteins comprising residues 22-442 (Fig. 4B, C). We verified the equivalence of the folding state of the three recombinant proteins by circular dichroism (CD), which revealed mean residual ellipticity (MRE) profiles consistent with the presence of a mix of α-helical and β-strand secondary structural elements in ATLs (Fig. 4D). We first tested whether the HSAN-causing mutations interfere with the GTPase activity of ATL3. We found that the GTPase activity of $ATL3^{WT}$ displayed significant cooperativity, as indicated by the sigmoidal relationship between the enzymatic activity and substrate concentration (Fig. 4E). Such cooperativity is in agreement with dimerization-dependence of the ATL3 GTPase activity. Similar analysis of the catalytic activity of $ATL3^{Y192C}$ and $ATL3^{P338R}$ revealed that these mutant proteins not only retain

the competence to hydrolyze GTP, but also maintain the ability to dimerize following GTP binding (Fig. 4E).

Following GTP hydrolysis, the ATL3 dimer is expected to undergo a conformational change whereby both molecules switch from their initial conformation, most likely resembling the extended structure, to a stable crossover dimer (Fig. 4A and Fig. S1) (Bian et al., 2011; Byrnes and Sondermann, 2011; Byrnes et al., 2013; Hu and Rapoport, 2016; Liu et al., 2015; O'Donnell et al., 2017; Saini et al., 2014). *In vitro*, these stable dimers form in the presence of the non-hydrolyzable GTP analog GTPγS and the transition state analog GDP.AlF_4^- (Morin-Leisk et al., 2011; Saini et al., 2014; Winsor et al., 2017). To examine oligomerization of the ATL3 22-442 proteins in solution, we performed size-exclusion chromatography (SEC) coupled to multi-angle laser light scattering (MALLS). While the SEC retention times correlate with the hydrodynamic volume of the particles, static light scattering allows molecular weight determination regardless of shape (Table S1) and therefore the possible oligomerization state of a given protein. We found that in the absence of nucleotide, all three proteins displayed the same SEC-MALLS profile, consistent with monomeric states averaging 48.1 kDa compared to the theoretical MW of 47.9 kDa (Fig. 4F and Table S1). In the presence of GDP, these profiles remained unchanged (Fig. 4F and Table S1). However, in the presence of GTP analogues, $ATL3^{WT}$ showed a clear tendency to dimerize, corroborating earlier findings (Bian et al., 2011; Byrnes and Sondermann, 2011; Byrnes et al., 2013; O'Donnell et al., 2017). At equilibrium, the presence of GTPγS separated $ATL3^{WT}$ into two distinct oligomeric states, with about half of the protein adopting a monomeric form and the remaining half a dimeric state (MW 92.7 kDa) (Fig. 4F and Table S1). GDP.AlF_4^- further shifted this equilibrium towards the dimeric species, reducing the monomeric form to about 30% (Fig. 4F and Table S1). Markedly, this oligomerization propensity was severely compromised in the case of $ATL3^{Y192C}$ and $ATL3^{P338R}$. In the presence of GTPγS, only a limited amount of $ATL3^{Y192C}$ and $ATL3^{P338R}$ was found in the dimer fraction (~20 %) (Fig. 4F and Table S1). While GDP.AlF_4^- again shifted the equilibrium towards dimers, it did so in decreased proportions with only 40% and 50% dimers for $ATL3^{Y192C}$ and $ATL3^{P338R}$, respectively (Fig. 4F and Table S1). Thus, we conclude that the mutations in ATL3 imprint a drastic reduction in the capacity of ATL3 to adopt a stable dimeric state following GTP hydrolysis. Since stable crossover dimer formation is a prerequisite for ATL-mediated membrane fusion (Saini et al., 2014; Winsor et al., 2017), this also explains our

earlier observations on defects in ER tubule fusion in cells expressing the pathogenic variants in ATL3 (Fig. 3A,B).

Mutations in ATL3 result in excessive ER tubule tethering

While being essential for membrane fusion, several studies have shown that stable crossover dimer formation is dispensable for membrane tethering (Saini et al., 2014; Winsor et al., 2017). Therefore, to test for the membrane tethering capacity of $ATL3^{Y192C}$ and $ATL3^{P338R}$, we replaced the transmembrane region of ATL3 with 10 histidines (termed ATL3 ΔTMR), which allows binding of the protein to Ni^{2+}-NTA containing liposomes (Fig. 5A, Fig. S5). Since the absence of transmembrane helices of ATL prevents membrane fusion (Liu et al., 2012; Saini et al., 2014), dynamic light scattering (DLS) can be used to analyze the tethering capacity of WT or mutant ATL3 ΔTMR *in vitro* by measuring the apparent increase in size of the proteoliposomes upon addition of GTP (Fig. 5A) (Liu et al., 2015). Indeed, $ATL3^{WT}$ proteoliposomes showed an increase in the mean radius upon the addition of GTP, from 163nm before to 192nm after addition of GTP, indicating steady-state tethering between a subset of liposomes at each given time point (Fig. 5B). Addition of EDTA reversed the increase in hydrodynamic radius, confirming that it was caused by tethering and not fusion (Fig. 5B). Unexpectedly, both disease-causing mutations in ATL3 did not only retain liposome-tethering activity, in fact they appeared hyperactive, resulting in a much more pronounced accumulation of tethered liposomes after the addition of GTP (Fig. 5B). These data suggest that while the mutant proteins fail to attain a stable crossover dimer in solution (Fig. 4F), their membrane tethering capacity is unaffected, showing that they do establish dimers in *trans* when associated with liposomes. Moreover, the defect in the fusion mechanism results in excessive or more stable tethering compared to $ATL3^{WT}$ (Fig. 5B).

To address whether this observation was relevant in cells expressing mutant ATL3 as well, we applied focused-ion beam scanning electron microscopy (FIBSEM) which allowed us to resolve the ultrastructure of the ER in large volumes at nanometer-scale resolution (Kremer et al., 2015). Volume EM images of cells overexpressing $ATL3^{WT}$ revealed that the ER in these cells exhibits a typical morphology hallmarked by an elaborate network of sheets (Fig. 6 upper panel and Video 4). Analysis of a similar region in the periphery of a HeLa cell expressing $ATL3^{Y192C}$ confirmed our earlier findings that the ER is sparsely connected in these cells and consists of long unbranched tubules (Fig. 6 middle panel and Video 5). In addition, we

observed several tubules that were attached laterally without the presence of a junction, as indicated by the differently colored ER tubules (Fig. 6 middle panel and Video 5). This became even clearer when analyzing the perinuclear region in the same cell expressing ATL3^{Y192C}. The collapsed ER -as shown in Fig. 1- consisted of a severely anomalous tangle of mostly ER tubules interspersed with a few ER sheets (Video 6). Reconstruction of a part of the ER tangle in this perinuclear region clearly showed the presence of long unbranched tubules that appear tethered laterally without being interconnected, again underscoring that mutant ATL3 is still capable of mediating membrane tethering, but not ER tubule fusion (Fig. 6 lower panel and Video 7). The loss of fusogenic capacity in these proteins appeared to result in excessive membrane tethering that has a major impact on ER morphogenesis in cells expressing mutant ATL3.

Aberrant ER membrane tethering in HSAN patient fibroblasts and neurons

So far, all our *in cellulo* data were generated from cells overexpressing WT or mutant ATL3. To exclude any possible artefact due to overexpression, we derived skin fibroblasts from a patient carrying the ATL3^{Y192C} mutation (Fig. 7). Staining for endogenous KDEL in these cells revealed discernable ER clustering, particularly in the perinuclear region (Fig. 7A). This became even more apparent using transmission electron microscopy. While control fibroblasts displayed a highly connected and well-spread ER, clusters of parallel-oriented unbranched ER membranes frequently occurred in the patient fibroblasts (Fig. 7B). These observations in HSAN patient-derived cells confirm that aberrant ER tubule tethering caused by mutations in ATL3 is relevant under endogenous ATL3 expression.

To assess whether this tethering is relevant for neurodegeneration, we expressed WT or mutant ATL3 in primary mouse cortical neurons using lentiviral transduction (Fig. 8). In these cells, the ER marked by ATL3-GFP was found to spread from a dense structure in the soma throughout the neurites regardless of whether WT or mutant ATL3 was expressed, indicating that the mutations do not prevent the generation of neurites or the spread of the ER therein (Fig. 8A). A large fraction of the neurons expressing ATL3^{Y192C} or ATL3^{P338R}, however, displayed a tangled ER structure (Fig. 8A, arrowheads), similar to what we observed in COS-7 or HeLa cells (Fig. 1 and Fig. 6). While such dense ER clusters were only observed in less than 10% of neurons overexpressing ATL3^{WT}, approximately 70% of cells expressing mutant ATL3 exhibited this phenotype, showing that this is a major hallmark of HSAN-causing mutations in

ATL3 (Fig. 8B). To show that these structures indeed represent an altered distribution of ATL3-GFP throughout the cells, we measured relative GFP intensities along single neurites starting from the center of the soma, which confirmed that neurons expressing mutant ATL3-GFP retained a larger fraction of the total GFP signal within this perinuclear ER structure compared to ATL3^{WT}-expressing cells (Fig. 8C). In summary, these data show that both in patient fibroblasts and in neuronal cells mutations of ATL3 lead to a collapse of the ER, further underscoring the physiological relevance of our findings.

DISCUSSION

In this study we have provided new cellular and mechanistic insights into how disease-related mutations in ATL3 interfere with the protein's functional cycle required for membrane fusion. Importantly, we show that such functional defects impact the structure and integrity of the ER both in cells overexpressing pathogenic variants of ATL3 and in patient derived fibroblasts. Indeed, the formation of new junctions through ER tubule fusion mediated by the Atlastin GTPases is essential for the continuous remodeling of the ER, defects in which cause axonal degeneration in diseases such as HSAN and HSP (Fischer et al., 2014; Guelly et al., 2011; Kornak et al., 2014; Zhao et al., 2001).

Recent studies on human ATL1-3 and *Drosophila* ATL (dATL) have proposed a model for ATL-mediated membrane fusion, although different studies have led to somewhat divergent conclusions. The most basic understanding of the fusion process arose from the observation of two distinct ATL1 dimer conformations in crystallization studies (Bian et al., 2011; Byrnes and Sondermann, 2011). In the extended structure, ATL1 adopts a head-to-head dimer conformation, where the 3HB middle domain interacts closely with the G domain within the same ATL1 molecule (Fig. S1A). Although it is now clear that this dimer can also occur in *cis* (Liu et al., 2015), the fact that the 3HB domains of both proteins point in opposite directions, suggested that this dimer could indeed form between two molecules on opposing membranes in a pre-fusion state (Bian et al., 2011; Byrnes and Sondermann, 2011). In the second dimer conformation, the 3HB domain has disengaged from the G domain and rotated along a hinge region formed by the flexible linker, resulting in a crossover dimer. The close proximity of both 3HB domains in this conformation suggests that this dimer occurs when both protomers reside in the same membrane, indicating a postfusion conformation (Bian et

al., 2011; Byrnes and Sondermann, 2011). More recently, a third, “tight crossover” dimer structure was revealed featuring a more extensive dimer interface that includes the G domain, the linker and the middle domains (Fig. S1B). This conformation was adopted in the presence of GMPPNP or GDP+AlF_4^-, representing the crossover dimer in the transition state (Byrnes et al., 2013). Different biochemical approaches suggested that the G domains of ATL1 dimerize upon GTP binding, and that GTP hydrolysis promotes the formation of a tight crossover dimer that subsequently converts into a more relaxed crossover dimer state (Bian et al., 2011; Byrnes and Sondermann, 2011; Byrnes et al., 2013). More recently, an alternative model was put forward in which GTP hydrolysis would occur in the monomer state, based on differences in timing during pre-steady state kinetics (O'Donnell et al., 2017). The authors proposed that the observed cooperativity in ATL enzymatic activity was thus not caused by dimerization-induced GTP hydrolysis, but rather by dimerization-stimulated Pi-release, which cannot be distinguished by the currently used read-outs for GTPase activity. It is at present unclear what drives the major conformational changes required for stable crossover formation and membrane fusion in this latter model.

Regardless of whether GTP hydrolysis occurs prior to G domain dimerization (Byrnes et al., 2013; O'Donnell et al., 2017), or rather ensues it (Winsor et al., 2017), our data show that the disease-causing variants do not interfere with the initial steps of the functional cycle leading up to G domain dimerization, nor do they affect the allosteric properties (Fig. 4E). However, the mutant proteins do show a different behavior in the steps following initial dimerization. The $ATL3^{Y192C}$ and $ATL3^{P338R}$ mutant proteins suffer from a reduced dimerization propensity in the presence of GTPγS or GDP+AlF_4^- (Fig. 4), suggesting that the mutants fail to establish the stable crossover dimer conformation following GTP hydrolysis. As this stable dimer is an absolute prerequisite to cross the energy barrier required for merging lipid bilayers (Winsor et al., 2017), failure to attain this conformation offers an attractive explanation for the inability of the mutant ATL3 to support membrane fusion, as reflected by the ER network connectivity deficit observed in COS-7 cells (Fig. 1-3).

In contrast to fusion, the preceding membrane tethering step does not depend on the stable crossover dimer (Liu et al., 2015; Morin-Leisk et al., 2011; Saini et al., 2014; Winsor et al., 2017). Interestingly, one of the most striking ER defects we could observe in cells expressing HSAN-causing mutations in ATL3, was the presence of extensive ER membrane tethering as revealed by volume EM. This unique phenotype was characterized by the

presence of bundles of ER tubules running in parallel over a large number of FIBSEM slices (Fig. 6 and Videos 6, 7). This aberrant tethering occurred mainly in a collapsed, high-density region of the ER near the nucleus, both in cell lines and in patient fibroblasts (Fig. 7). Moreover, ER tangling was also detected in primary neurons expressing the disease-causing variants in ATL3 (Fig. 8), indicating that the aberrant tethering caused by these mutations has physiologically relevant consequences, interfering with the organization of the ER network in neuronal cells. Although we currently do not have direct structural data to rationalize the underlying mechanism, we hypothesize that HSAN-causing mutations in ATL3, located in the interface between the G and the 3HB domain, prevent the protein from proceeding through its functional cycle following trans-dimerization and GTP hydrolysis. This stalling can in turn result in prolonged membrane tethering. These interactions were not retrieved in our SEC-MALLS experiments, indicating that they are transient or might require further stabilization by membrane association and the 2-dimensional spatial confinement of the membrane (Winsor et al., 2017). Indeed, our *in vitro* tethering assay confirmed that both disease-causing mutations in ATL3 promote excessive liposome tethering compared to the WT protein (Fig. 5).

Together, our findings are in agreement with a model in which GTP binding and hydrolysis drives ER membrane tethering through ATL trans-dimerization (Fig. 9A, B). Subsequent membrane fusion relies on the formation of a stable crossover dimer bringing the membranes in close apposition, resulting in a new three-way junction (Fig. 9B, C). While the HSAN-causing mutations in ATL3 do not abrogate GTP binding or hydrolysis, the mutant proteins fail to completely execute the subsequent conformational changes required to form a stable crossover dimer, rendering the mutant ATL3 fusion-deficient (Fig. 9D). Underscoring the relevance of this stable crossover conformation to reset the protein for a new round of tethering and fusion (O'Donnell et al., 2017), the inability of both mutants to proceed to this step of the ATL functional cycle causes aberrant membrane tethering that leads to a partial collapse of the ER network, strongly affecting ER dynamics.

ATL1 is the predominant isoform in the nervous system (Kornak et al., 2014; Rismanchi et al., 2008), and also the Atlastin with the highest intrinsic fusogenic capacity (Hu et al., 2015; O'Donnell et al., 2017). Therefore, haploinsufficiency as a consequence of the loss of ATL1 fusion activity is thought to underlie the HSP or HSAN phenotype in patients (Ulengin et al., 2015). ATL3 on the other hand was found to be a much weaker fusogen (O'Donnell et al., 2017), and loss of ATL3 has only marginal effects on overall ER morphology (Hu et al., 2015).

Therefore, in the case of the dominant missense mutations in ATL3 causing HSAN, haploinsufficiency is far less likely and the partial collapse of the ER network caused by the excessive membrane-tethering in the ATL3^{Y192C} and ATL3^{P338R} mutants might have a much higher impact on neuronal functioning. Not only does this tethering disturb normal ER membrane dynamics, it likely interferes with the organization of different ER subdomains playing various roles in neuronal homeostasis (English and Voeltz, 2013).

MATERIALS & METHODS

Cloning and plasmids

All ATL3-expressing vectors were created using Gateway recombination system (ThermoFisher Scientific). The WT and Y192C ATL3 cDNA was amplified from a previously reported vector (Kornak et al., 2014) using primers extended with attB sites (forward primer: GGGGACAAGTTTGTACAAAAAAGCAGGCTATGTTGTCCCCTCAGCGAGTG; reverse primer: GGGACCACTTTGTACAAGAAAGCTGGGTCTTGAGCTTTTTTATCCATGGATGGTCTTCC), and subsequently cloned into a pDONR221 using the BP clonase (ThermoFisher Scientific). The P338R open reading-frame (ORF) was synthesized by Genscript and cloned in the same way. After sequence validation, expression plasmids were created using the LR clonase (ThermoFisher Scientific) in combination with the pLenti6/EGFP-Dest to allow C-terminal GFP-tagging. Lentiviral particle production for ATL3-GFP expression in cortical neurons was performed as previously described (Salmon and Trono, 2006). ATL3-mCherry expression plasmids were created through multisite-gateway cloning. Here, the mCherry ORF was amplified and subcloned into the pDONR-P2RP3. Expression vectors were created by combining the aforementioned ATL3 entry clones with the mCherry C-terminal entry clone and a mock N-terminal entry clone in the LR reaction. For recombinant protein expression in *E. coli*, WT and mutant ATL3 ORFs were truncated to express amino acids 22-442, and cloned in a pET15 vector allowing expression of a thrombin-cleavable C-terminal His(6)-tag using Gateway cloning. All vectors were sequence verified. The pCI-mRubyKDEL vector was a gift from Dr. Jörg Wiedenmann (Kredel et al., 2009). The PA-GFP-KDEL vector was a gift from Dr. Vicky Claire Jones (Jones et al., 2009).

Cell lines

A culture of primary dermal fibroblast cells from a patient with a c.575A>G (p.Tyr192Cys) mutation in the ATL3 gene was generated by mechanical dissection and enzymatic digestion tissue from a 3 mm diameter punch biopsy. The fibroblasts were seeded on cell culture treated 6-well plates followed by expansion in Chemicon FibroGRO-LS medium (Merk Millipore, Darmstadt) following the manufacturer's instructions. The cells were passaged once per week with 0,25 % Trypsin-EDTA (ThermoFischer Scientific, Dreieich, Germany) and at passage 3 checked for absence mycoplasma contamination with the Universal ATCC Mycoplasma Detection Kit (LGC standards GmbH, Wesel, Germany). The procedures were approved by the Ethics Committee of the Christian-Albrechts University Medical School under the reference number A 145/11.

All cell lines were cultured in a 37°C and 5% CO_2 atmosphere. Human Skin Fibroblasts were cultured in FibroGro medium (Millipore). COS-7 and HeLa cells were cultured in high-glucose DMEM (ThermoFisher Scientific) supplemented with 10% fetal bovine serum (FBS) (ThermoFisher Scientific).

ER morphology and fusion success rate

Given their flatness and well-spread tubular ER network, COS-7 cells are ideal for live-cell imaging of the ER. The cells were seeded in glass-bottom 24-well plates (Eppendorf) and allowed at least 24h to attach. At a cell density of >50%, transient transfection with empty vector or ATL3-GFP and mRuby-KDEL was performed using Lipofectamine-LTX (ThermoFisher Scientific) according to the manufacturers protocol. 24h after transfection, medium was replaced by FluoroBrite™ DMEM (ThermoFisher Scientific) supplemented with 10% FBS and 2mM L-glutamine (ThermoFisher Scientific). The cells were imaged on the UltraVIEW VoX spinning disk confocal microsocope (Perkin Elmer), equipped with a Hamamatsu C9100-50 EMCCD camera and a 40x/1.3 oil immersion objective, controlled through the Volocity software. ATL3-GFP and mRuby-KDEL were imaged using a 488nm and 555nm excitation laser, respectively. Both channels were sequentially imaged using a 400ms exposure time at a frame rate of $1sec^{-1}$. Image analysis was performed using ImageJ/FIJI (Schindelin et al., 2012; Schneider et al., 2012). The first frame of the mRuby-KDEL channel was used for ER morphology analysis (Fig. 1C-E). Surface areas of the outermost polygons of each cell were measured manually and used as a measure of 'ER sparsity'. To determine the threeway junction density of the peripheral ER, images were cropped to avoid the incorporation of

perinuclear ER where branch points cannot be accurately determined. After Gaussian blurring, background subtraction and intensity thresholding, the ImageJ 'Skeletonize' function was used to obtain the number of branch points (Arganda-Carreras et al., 2010). To assess ER tubule fusion efficiency, events where the tip of an extending tubule encounters another ER tubule were monitored. When this encounter results in a new branch point, it was recorded as a successful fusion event. When the tubules detach shortly after the encounter, it was considered a failed fusion event. The success rate is measured as the fraction of events resulting in successful fusion.

Immunofluorescence microscopy

HeLa and COS-7 cells were cultured, seeded on coverslips and transfected with mRuby-KDEL or ATL3-mCherry as described above. 24 hours after transfection, the cells were fixed in 2% paraformaldehyde (PFA) and 4% sucrose (Sigma Aldrich) in phosphate buffered saline (PBS). Human skin fibroblasts were seeded on coverslips and fixed in 4% PFA in PBS after at least 24 hours in culture. After washing, fixed cells were permeabilized with 0.1% Triton-X-100 in PBS and coverslips were placed in blocking solution (2% FBS and 2% BSA in PBS). Cells were incubated overnight at 4°C with primary antibodies in 10% blocking solution: rabbit-anti-Giantin 1:1000 (Covance); mouse IgG2a-anti-KDEL 1:100 (Enzo). Goat-anti-rabbit or goat-anti-mouse secondary antibodies labelled with Alexa Fluor 488 (ThermoFisher Scientific) were used at a 1:500 dilution. After washing in PBS, cells were incubated with Hoechst 33342 (ThermoFisher Scientific) for 10mins at room temperature prior to mounting the coverslips using DAKO mounting medium. Imaging was performed on a Zeiss LSM700 confocal microscope using a 20x/0.8 plan-apochromat objective for the Golgi staining, or a 40x/1.3 Plan-Neofluar objective for the ER staining. Image analysis was done in ImageJ or CellProfiler software (Kamentsky et al., 2011; Schindelin et al., 2012).

Photo-activatable GFP imaging

COS-7 cells were cultured as described above. After seeding in an 8-well µslide (ibidi), cells were co-transfected with ATL3-mCherry and PA-GFP-KDEL using Lipofectamine-LTX, as above. The medium was replaced by Fluorobrite™ DMEM (ThermoFisher Scientific) supplemented with 10% FBS and 2mM L-glutamine (ThermoFisher Scientific) and live cells were imaged on the Zeiss LSM700 microscope equipped with a 37°C and 5% CO_2 incubation chamber and a

40x/1.3 Plan-Neofluar objective, and controlled through the Zen software. The 555nm laser was used to image ATL3-mCherry-positive cells. PA-GFP-KDEL was activated using the 405nm laser at 100% and imaged for 90s using the 488nm laser at a frame rate of 1 frame per second. To reduce inter-cell variability, the PA-GFP activation was performed in a perinuclear region with a similar density of the ER in each cell. Image analysis was performed in ImageJ (Schindelin et al., 2012; Schneider et al., 2012) and R (http://www.R-project.org/). The fluorescence intensity was measured in regions of interest (ROIs) at fixed distances from the activation region. The signal was normalized, setting the initial fluorescence to zero and the maximum fluorescence to 1 for each ROI. In R, exponential curves were fitted to the normalized data, from which the $T_{1/2}$ was determined as the timepoint at which the fluorescence intensity reached 50% of the maximum value of the exponential fit.

Transmission electron microscopy

Human skin fibroblasts were cultured and seeded on glass coverslips as described above. Cultures were fixed in 4% paraformaldehyde and 2.5% glutaraldehyde in 0.1 M sodium cacodylate buffer, pH 7.2 for 4 hours at RT followed by fixation overnight at 4°C. After washing, cells were subsequently dehydrated through a graded ethanol series, including a bulk staining with 1% uranyl acetate at the 50% ethanol step followed by embedding in Spurr's resin.
Ultrathin sections of a gold interference color were cut using an ultra-microtome (Leica EM UC7), followed by a post-staining in a Leica EM AC20 for 40 min in uranyl acetate at 20 °C and for 10 min in lead stain at 20 °C. Sections were collected on formvar-coated copper slot grids, which were viewed with a JEM 1400plus transmission electron microscope (JEOL) operating at 70 kV. Image analysis was done using ImageJ.

Volume electron microscopy

For volume-EM imaging, HeLa cells were cultured as described above. The cells were seeded in 35mm imaging dishes with a gridded coverslip (MatTek) and transfected with ATL3-GFP using Lipofectamine-LTX. Prior to fixation, transfected cells were imaged with the 488nm laser on a Zeiss LSM700 confocal microscope. Using the 10x objective and the 'stitching' mode in the Zen software, DIC images were obtained to determine to position of cells of interest in the alphanumerically labelled grid. These ATL3-GFP-positive cells were then also imaged using the 40x objective to obtain the overall cell morphology in more detail. Then, cells were fixed using

1.5% PFA and 2.5% glutaraldehyde in wash buffer (0.15M sodium-cacodylate buffer pH 7.4, containing 2mM calcium chloride). Fixation was performed at room temperature for 1 hour. Cells were further processed for imaging on the Zeiss Auriga Crossbeam system as described (Knott et al., 2011). FIBSEM imaging at a 5x5x5 nm voxel size was performed as previously described (Kremer et al., 2015). Registration, segmentation and 3D reconstruction was done using ImageJ and IMOD (http://bio3d.colorado.edu/imod/).

Primary cortical neuron cultures

Cortical neurons extracted from E15.5 C57BL/6 embryos were cultured in neurobasal medium (ThermoFisher Scientific), supplemented with 2% fetal bovine serum (ThermoFisher Scientific), 2mM glutamine, 100µg/mL penicillin-streptomycin, 2% B27 and 4g/L d-glucose on poly-D-lysine coated coverslips. After 4hours incubation at 37°C and 7% CO_2, appropriate lentivirus was added to the medium. Cultures were kept for at least 5 days before fixation and staining, as described above. Imaging was done on a Zeiss LSM700 microscope with a 40x/1.3 Plan-Neofluar objective controlled through the Zen software.

ER tangling in ATL3-GFP expressing neurons was visually scored by the presence of structures with unusually high GFP fluorescence compared to the GFP-intensity in the rest of the soma and the neurites. To quantify the spread of ATL3-GFP within the neurons, overlapping images were acquired using an automated Nikon Ti wide-field microscope with 20x Plan Apo 0.75 NA objective and DS-Qi2 CMOS camera (Nikon) and stitched together using the Nikon NIS Elements software, resulting in large tiled images of 6mm by 6mm with 364nm x 364nm pixels, which were used in Fiji (Schindelin et al., 2012) for image analysis. To plot nuclear stain and GFP signal intensity, a segmented line starting in the center of the nucleus was drawn to trace a single neurite of individual ATL3-GFP expressing cortical neurons. For each position along this line, the GFP fluorescence intensity was normalized to the total GFP signal within the trace (area under the curve). Graphpad Prism 7 was used to plot the normalized fluorescence intensity in function of the corresponding pixel position.

Generation of a structural model for ATL3

The model used to depict the overall three-dimensional structure and the location of the clinical mutations of ATL3 in the parallel conformation were generated using MODELLER (Webb and Sali, 2016) within the Chimera environment (Pettersen et al., 2004). As input, a

ClustalW (Larkin et al., 2007) alignment of ATL3 and ATL1 were given along with structural templates of ATL1 (4IDP for the parallel model (Byrnes and Sondermann, 2011; Byrnes et al., 2013). The final images were generated and rendered in PyMol (Schrödinger, 2015). The structure for ATL3 in the extended conformation is represented by the recently solved crystal structure by O'Donnell et al (pdb 5VGR) (O'Donnell et al., 2017).

Protein expression and purification

Recombinant WT and mutant ATL3 were expressed in *E. coli* and purified using immobilized metal affinity chromatography (IMAC) and size-exclusion chromatogfaphy (SEC). Specifically, pET15b vectors bearing the corresponding WT and mutant ATL3 ectodomain sequences, coding for residues 22 till 442 and an additional C-terminal thrombin cleavable HIS(6)-tag, were transformed into *E. coli*. Small scale expression tests showed that soluble expression of WT ATL3 was best achieved in the standard BL21 (DE3) strain, while for both mutants this was in the Rosetta 2 strain. Expression cultures were started in lysogeny broth (LB) supplemented with carbenicilline (Cb), induced with Isopropyl β-D-1-thiogalactopyranoside (IPTG, 1mM final concentration) at OD 0.6-0.8, and grown overnight at 26°C shaking at 200 rpm. The next day, the bacterial pellet was harvested (centrifuged for 10' at 10,000 g) and lysed by sonication (30" on, 30" off, 4' total on time at 60 % amplitude, Qsonica Q500). For all purification steps, a low-salt tris buffer, supplemented with 10% glycerol, was used (20 mM tris pH 8.5, 50 mM NaCl and 10 % glycerol). The extract was cleared from debris by centrifugation (45' at 50,000 g) and filtration (0.2 µm bottletop filter). Next, recombinant ATL3 was purified from the extract by Immobilized Metal Affinity Chromatography (IMAC) (HisTrap 5ml, GE Healthcare) exploiting the nickel binding HIS(6)-tag. Protein was eluted with imidazole (200 mM) and immediately desalted by size exclusion chromatography (SEC) (HiPrep 26/10 Deslating, GE Healthcare). The HIS(6)-tag was cleaved with thrombin (Restriction grade thrombin, Millipore) overnight at 20°C. To remove the HIS(6)-tag and co-purified contaminants, negative IMAC was performed. The flow-through, now containing ATL3, was concentrated to a final volume of 4 ml and injected on a SEC column (Superdex 75 pg, HiLoad 16/600, GE Healthcare). All chromatographic steps were performed on an ÅKTA purification station (ÅKTApurifier, GE Healthcare). Eluted fractions containing ATL3 were pooled, concentrated and loaded on the SEC again as a final polishing purification step. The final protein solution was diluted or concentrated to 1 mg/ml, aliquoted, flash-frozen in liquid nitrogen and stored at -80°C until

further use. Samples (2.4 µg) were run on SDS-PAGE (TGX Stain-free FastCast, 15 %, BioRad) and visualized with coomassie brilliant blue to verify the purified product.

Circular Dichroism

To verify the folding state of recombinant ATL3 wildtype and mutant proteins we carried out measurements by circular dichroism (CD). Unfolded, alpha-helical or beta-strand structures have distinct CD profiles, with maximum differential absorbance of left- and right-handed circular polarized light at 195 nm (unfolded), 208 nm and 222 nm (α-helix) or 218 nm (β-sheet) (Greenfield, 2006). The recombinant ATL3 proteins (WT, Y192C and P338R) where thawed (1 mg/ml) and diluted 1/5 in a more CD compatible buffer (20mM K_2HPO_4/KH_2PO_4, 50mM NaF) to a final volume of 200 µL and concentration of 0.2 mg/ml. The samples were transferred to a 1 mm quartz cuvette and analyzed with the CD spectrometer (25°C, wavelength range: 195-260 nm, resolution 1 nm, 1 s averaging time, Model 410, AVIV biomedical). Data were analyzed with CDNN software (v3.0) (Böhm, 1997).

GTPase activity

GTPase activity was measured using the EnzCheck phosphate assay kit (ThermoFisher Scientific). 100µL reactions were prepared in a 96well plate (Greiner) according to the manufacturer's recommendations, using 0.1µM ATL3 WT, Y192C or P338R in each reaction. After 10min incubation at room temperature, variable concentrations of GTP were added to start the reaction and absorbance at 360nm was measured at an interval of 8sec for 15min on a Synergy HT plus spectrophotometer. From these reads, the initial velocities (V) were determined, and plotted in function of the substrate concentration. The data were analyzed using non-linear regression and fitted to an allosteric sigmoidal curve in Graphpad Prism 7.

SEC-MALLS

Size exclusion chromatography - Multi-Angle Laserlight Scattering (SEC-MALLS) experiments were performed on a sequential setup encompassing the following: Degasys degasser (Gynkotek), 1260 Infinity HPLC pump (Agilent), Superdex 200 Increase 10/300 GL SEC column (GE Healthcare), SPD-10A UV-VIS detector (Shimadzu), miniDAWN TREOS light scattering detector (Wyatt) and Optilab T-rEX refraction index detector (Wyatt). Prior to injection, protein samples (100 µL at 1 mg/ml) were incubated for 90' at room temperature with one of

the following reagent combinations: 20mM $MgCl_2$, 20mM $MgCl_2$ and 2.5mM GDP (Sigma), 20mM $MgCl_2$ and 2.5mM GTPγS (Sigma), or 20mM $MgCl_2$, 2.5mM GDP (Sigma), 2mM $AlCl_2$ and 20mM NaF. Samples were run at 0.5 ml/min and the running buffer was the same as the storage buffer (20 mM tris pH 8.5, 50 mM NaCl and 10 % glycerol) with the addition of 20 mM of $MgCl_2$ to ensure its continuous presence. As a calibration reference, bovine serum albumin (Albumin standard, Thermo Scientific) was used. Data were recorded and analyzed using the ASTRA software package (Wyatt, v6.1).

Dynamic light scattering

ATL3 ΔTMR constructs were expressed and purified as described above, with exception of the negative IMAC step which was omitted for this construct. Ni^{2+}-NTA containing liposomes were prepared by pore extrusion. A lipid mixture composed of 95% POPC (Sigma)/5% DGS-NTA (Ni^{2+}) (Avanti) dissolved in chloroform were dried in glass tubes by Argon gas, rehydrated to 1mg/ml into buffer (20mM Tris, 50 mM NaCl, 10% glycerol) and filtered 20x through 0.2µm diameter polycarbonate membranes (Nucleopore). Timecourse DLS measurements were performed in a DynaPro plate reader-II (Wyatt technology) using reactions consisting of 100µg/µl liposomes and 0.2µM ATL3 ΔTMR in 20mM Tris, 50 mM NaCl, 10% glycerol and 5mM $MgCl_2$. To promote ATL3-mediated dimerization 4mM GTP was added at the indicated time (~30 minutes). To stop tethering 100mM EDTA was added at the indicated time (~145 minutes). Reactions were kept at 37°C. Measurements were taken with the highest frequency possible (every ~6,5 minutes).

Statistical analysis

All statistics was performed using the Graphpad Prism 7 software. Specific tests used are indicated in the figure legends.

Acknowledgements:

M.K. is supported by a predoctoral fellowship of the Fund for Scientific Research (FWO-Flanders, Belgium) and a short term EMBO fellowship. S.D. is supported by a predoctoral fellowship from the Flemish Agency for Innovation and Entrepreneurship (VLAIO). L.A.-S. is an EMBO Long Term fellow and is supported by Marie Curie Actions. F.J.M. is supported by grants

from the BMBF (13GW0128A and 01GM1513D) and from the Deutsche Forschungsgemeinschaft (DFG MU 3231/3-1). H.T.M. is funded by the Medical Research Council UK (grant number U105178795). The research of V.T. is supported by the FWO, University of Antwerp, the Hercules Foundation, the "Association Belge contre les Maladies Neuro-Musculaires" (ABMM) and the EU FP7/2007–2013 under grant agreement number 2012-305121 (NEUROMICS). The research program of S.J. is supported by the FWO, Ghent University and GROUP-ID. S.N.S. is supported by the FWO, the Hercules Foundation, and the VIB. The Zeiss Auriga was acquired through a CLEM grant from Minister Ingrid Lieten to the VIB Bio Imaging Core. Special thanks to Sonia Bartunkova, Michiel De Bruyne, Isabel Pintelon and Peter Verstraelen for advice and technical support. Also thanks to Chris Guérin for advice in image processing. Thanks to Vicky Claire Jones and Joerg Wiedenmann for providing plasmids. Molecular graphics and analyses were performed with the UCSF Chimera package. Chimera is developed by the Resource for Biocomputing, Visualization, and Informatics at the University of California, San Francisco (supported by NIGMS P41-GM103311).

FIGURE LEGENDS

Fig. 1: **Mutations in ATL3 abate ER network connectivity.** A) COS-7 cells were transfected with ATL3-GFP (green) and mRuby-KDEL as an ER marker (magenta). A higher magnification image of the boxed area is shown in the right panel. Scale bar = 10µm. B) The mRubyKDEL ER-marker was imaged in COS-7 cells transfected with empty vector, $ATL3^{WT}$, $ATL3^{Y192C}$ or $ATL3^{P338R}$, as indicated. A higher magnification of the boxed area is shown. Scale bar = 10µm. C) The number of threeway junctions per cell area (junction density) was quantified as a measure of peripheral ER connectivity. Boxplots show the median and the 1st and 3rd quartiles. Whiskers indicate the minimum/maximum values. D) ER sparsity was measured as the average surface area of the polygons formed by ER tubules. Mean +/- SEM is plotted. Statistical analysis in C) and D) was performed using one-way Anova followed by Tukey's multiple comparisons test. *: P<0.05; ***: P<0.001; n = 22-32 cells per genotype.

Fig. 2: **ER continuity is not lost in ATL3 mutant cells**. ER-targeted photo-activatable GFP (PA-GFP-KDEL) was imaged at 1 frame per second in COS-7 cells transfected with $ATL3^{WT}$, $ATL3^{Y192C}$ or $ATL3^{P338R}$, as indicated (see Video 1). A) PA-GFP-KDEL was activated in a small area next to the nucleus, after which the activated fluorophores diffuse through the lumen of the entire ER network. Fluorescence intensity color code of the PA-GFP-KDEL is shown on the top left. The frame just prior to activation is indicated as t=0sec and the frame immediately following activation as t=1sec. To clearly show the peripheral ER network, the last frame is also shown as a high-contrast, inverted grayscale image. Scale bar = 10µm. B) The increase in fluorescence intensity over time was measured in regions of interest at fixed distances (8, 12, 16 and 20µm) from the site of activation (Fig. S4). Ribbon plots show the mean fluorescence intensity ± SEM for cells expressing $ATL3^{WT}$ (red), $ATL3^{Y192C}$ (blue) and $ATL3^{P338R}$ (green). C) The half-time to reach maximum intensity was extracted by fitting an exponential curve to the phase of fluorescence increase in each region of interest, as highlighted in Fig. S4. Mean ± SEM is plotted and statistical analysis was performed using two-way Anova followed by Tukey's multiple comparisons test. *: P<0.05; **: P<0.01; ****: P<0.0001; n = 40-75 regions of interest per distance in 10-17 cells per genotype.

Fig. 3: **ATL3 mutations cause loss of ER fusion efficiency.** Live cell imaging was performed to examine the effect of mutant ATL3 expression on ER tubule fusion. A) The mRubyKDEL ER-

marker was imaged at a frame rate of 1 sec^{-1} in COS-7 cells transfected with empty vector, $ATL3^{WT}$, $ATL3^{Y192C}$ or $ATL3^{P338R}$, as indicated (see Videos 2,3). Arrowheads mark the tips of extending tubules. An encounter between the extending tubule and another one is marked by an asterisk. Arrows mark the tip of a retracting tubule. Scale bar = 10µm. B) The success rate of tubule fusion was determined as the fraction of tubule encounter events (as marker by asterisks in A) that result in the formation of stable junctions. Events where tubules retract after an encounter (as indicated by arrows in A) were counted as failed fusion events. Boxplots and whiskers indicate mean and minimum/maximum values. Statistical analysis was performed using one-way Anova, followed by Tukey's multiple comparisons test. **: P<0.01; ****: P<0.0001; n = 8-11 cells per genotype.

Fig. 4: **Mutations in ATL3 impair GTP-dependent dimerization.** A) The main ATL3 structures are presented in cartoon representation. Residues in the zoom boxes are represented in the "stick" format. The "tight crossover" conformation of ATL3 was based on ATL1 structures (pdb 4IDP) and is shown in light (G-domain) and dark (M-domain) teal. In orange is the recently reported structure of ATL3 in the "extended" conformation (pdb 5VGR). The Cα atoms of residues Y192 and P338 are marked as red spheres in the main structure. The same residues are colored red in the zoom boxes. B) The functional domains of ATL3 and the locations of the mutated residues in the full-length ATL3 protein is shown above (3HB = three helix bundle; TM = transmembrane domain). Below, the ATL3 22-442 fragment that was expressed and purified from E. coli. C) Purified WT and mutant ATL3 were loaded and run on an SDS-PAGE, and visualized using coomassie brilliant blue. Bovine serum albumin (BSA) was used as a standard on the right and a molecular weight marker (M) is shown on the left. D) CD signal is expressed as mean residual ellipticity (MRE) and corresponds to the amount of differential absorbance of right- and left-handed circular polarized light. Alpha-helical structures typically absorb at 208 and 222 nm. Beta-strands typically absorb around 218 nm. Disorders or unfolded peptides absorbance near 195 nm. The curves corresponding to the different proteins are marked with squares ($ATL3^{WT}$), triangles ($ATL3^{Y192C}$) and circles ($ATL3^{P338R}$). E) GTPase activity of ATL3 22-442 of WT (squares), Y192C (triangles) and P338R (circles) ATL3 at increasing substrate concentration, fitted to an allosteric sigmoidal curve. F) Oligomerization of purified WT (left), Y192C (middle) and P338R (right) ATL3 22-442 was analyzed using SEC-MALLS. The differential refractive index (dRI, left axis, continuous curve) and molecular weight

(right axis, discrete curves above peak maxima) are plotted in function of the SEC retention time. The theoretical mass of the ATL3 monomer and dimer are marked by the dashed horizontal lines. The curves corresponding to the different conditions to which the protein was subjected prior to injection are marked with squares (Mg^{2+}), diamonds (Mg^{2+} GDP), triangles (Mg^{2+} GTPγS) and circles (Mg^{2+} GDP.AlF_4^-).

Fig. 5: **Mutations in ATL3 cause excessive membrane tethering *in vitro.*** A) To analyze membrane tethering activity, ATL3 ΔTMR was immobilized on Ni^{2+}-NTA containing liposomes through its 10xHis stretch. B) The increase in apparent hydrodynamic radius of the proteoliposomes upon tethering was measured using dynamic light scattering. Tethering was induced by adding 4mM GTP and blocked by the addition of 100mM EDTA at the indicated time points.

Fig. 6: **Mutations in ATL3 result in aberrant tethering of unbranched tubules.** High-resolution volume electron microscopy of HeLa cells expressing WT (upper row) or mutant (middle and lower rows) ATL3 was performed using focused ion-beam scanning electron microscopy (FIBSEM). A representative section of each cell is shown on the left and a higher magnification of the marked area is shown in the middle column. A 3D model obtained by manual segmentation of a fraction of the ER (as marked in color on the FIBSEM slice) and reconstruction using IMOD is shown on the right. Differently colored tubules indicate that these are discontinuous within the reconstructed volume. See also Videos 4-7. Scale bars = 500nm. N = nucleus.

Fig. 7: **ER tubule clustering is present in HSAN patient fibroblasts.** A) Human skin fibroblasts of control (above) or HSAN-I (below) individuals, immunostained for endogenous KDEL as an ER marker. Hoechst nuclear stain is shown in blue. Scale bar = 20µm. Higher magnifications of the boxed areas are shown. B) TEM images of control fibroblasts (above) and patient fibroblasts (below). Higher magnifications of the marked areas are shown on the right, with the ER marked in red.

Fig. 8**: ER tangling is observed in primary cortical neurons expressing mutant ATL3.** A) Primary mouse cortical neurons were transduced with ATL3-GFP and Hoechst nuclear stain is

shown in blue. Higher magnifications of ATL3-GFP in the boxed areas are shown in a fluorescence intensity color code as indicated in C. Arrow heads mark dense ER clusters in the mutant neurons. Scale bar = 20µm. B) The fraction of cells expressing WT or mutant ATL3 displaying ER tangling (as marked by arrowheads in A) was determined in 3 independent cortical neuron isolations (n=39-53 cells). Mean ± SEM is plotted. ***: $P < 0.001$ in a one-way Anova test. C) Normalized GFP and nuclear stain fluorescence intensity are plotted in function of the position along a line segment that traces a single neurite and starts in the center of the nucleus. A 'straightened' version of such a 30µm neurite tracing from the cells shown in A, is shown for each genotype below the graph. Mean ± SEM is plotted (n=30-35 cells).

Fig. 9: **Model for ATL3-mediated membrane fusion and the effects of HSAN-causing mutations in this mechanism.** A) ATLs in opposing membranes are monomeric in their apo-form, allowing the binding of GTP. B) Binding and hydrolysis of GTP promotes a striking conformational change, whereby the 3HB middle domains (blue) rotate along a hinge region (green), resulting in a tight crossover dimer that promotes membrane merging. C) The crossover dimer relaxes after the release of Pi, which is most likely followed quickly by resolving the dimer into monomers. D) The HSAN-causing mutations in ATL3 interfere with the conformational change following GTP hydrolysis. Although the proteins do adopt a conformation that promotes membrane tethering, they are incapable of inducing full membrane fusion.

SUPPLEMENTARY MATERIAL

Fig. S1: **ATL dimer conformations.** The "extended" (A) and "tight crossover" (B) conformations of ATL3 were based on ATL1 structures (pdb 3Q5E and 4IDP resp.). Bound nucleotides are shown in purple. A) The extended dimer conformation, in which only the G domains take part in the dimerization interface, represents the prefusion state. B) In the tight crossover conformation, the 3HB domain of each protomer as detached from its respective G domain, and rotated approximately 90°, resulting in a crossover dimer with an extensive dimer interface. The proximity of both 3HB domains suggests this dimer only exists when both proteins reside in the same membrane, indicating a postfusion conformation.

Fig. S2: **ATL3 overexpression in COS-7 cells.** COS-7 cells transiently transfected with empty vector (EV) as control, or GFP-tagged versions of $ATL3^{WT}$, $ATL3^{Y192C}$ or $ATL3^{P338R}$. ATL3 was detected using western blot, showing comparable expression of the three versions of ATL3-GFP, as well as equal levels of endogenous ATL3 in all lanes.

Fig. S3: **Golgi network morphology is unaffected in mutant ATL3 cells**. COS-7 cells expressing ATL3-mCherry (red) were immunostained for Giantin (green) as a Golgi marker. A merge is shown with the nucleus in blue and the cell outline marked in white. Scale bar = 20µm.

Fig. S4: **PA-GFP-KDEL analysis**. PA-GFP-KDEL was activated in a small region of interest (ROI) near the nucleus (white square). Fluorescence intensity was measured at discrete distances from the site of activation, in multiple ROIs per distance per cell. A very rapid increase towards maximum fluorescence intensity was observed in ROIs at 8µm from the site of activation (yellow), whereas at distances further from the photoactivation site maximum intensity is reached later (blue, red and green boxes and curves for 12µm, 16µm and 20µm respectively). Raw fluorescence intensities were normalized to the maximal value within each ROI, and an exponential curve was fitted to the growth and plateau phase of the response, from which the average time to reach half of the maximum fluorescence ($T_{1/2}$) was determined for each distance. Scale bar = 10µm.

Fig. S5: **ATL3 dTMR expression.** Purified WT and mutant ATL3 dTMR were loaded and run on an SDS-PAGE, and visualized using coomassie brilliant blue. A molecular weight marker (M) is shown on the left.

Video 1: **Photoactivatable GFP-KDEL**. PA-GFP-KDEL was transiently expressed in COS-7 cells, along with ATL3-mCherry as indicated in Fig. 2. Imaging was performed at 1 frame per second, and 5 frames were recorded prior to photoactivation of the PA-GFP-KDEL in a small region near the nucleus.

Video 2: **Successful tubule fusion.** mRuby-KDEL was transiently transfected in COS-7 cells to label the ER, along with ATL3-GFP as indicated in Fig. 3. To monitor tubule encounter events, live-cell imaging was performed at 1 frame per second. In this example, a new threeway junction is formed upon encounter between the extending tubule at the far left and the opposing tubule.

Video 3: **Failed tubule fusion.** As in Fig. 3 and Video 2, COS-7 cells were transfected with mRuby-KDEL and imaged at 1 frame per second. In this example, the tubule encounter occurring at the center of the view fails to result in a new junction, and the extending tubule eventually retracts.

Video 4: **ER ultrastructure in an ATL3^{WT}-expressing HeLa visualized using volume electron microscopy.** Focused-ion beam scanning electron microscopy (FIBSEM) was performed on a HeLa cell expressing WT ATL3-GFP. This video shows a digitally resliced version of the original image stack, and a 3D model of a portion of the ER in green, as in Fig. 5.

Video 5: **ER tubule tangling and loss of network complexity in a HeLa cell expressing ATL3^{Y192C}.** Focused-ion beam scanning electron microscopy (FIBSEM) was performed on a HeLa cell expressing Y192C ATL3-GFP. A 3D reconstruction of a portion of the ER is shown as in Fig. 5.

Video 6: **ER tubule tangling and loss of network complexity in a HeLa cell expressing ATL3^{Y192C}.** Focused-ion beam scanning electron microscopy (FIBSEM) was performed on a

HeLa cell expressing Y192C ATL3-GFP. This video shows a perinuclear region of this cell (Fig. 5), revealing a tangle of ER membranes that represents the collapsed ER seen in Fig. 1.

Video 7: **Extensive ER tubule tangling in a perinuclear region of a HeLa cell expressing ATL3^{Y192C}.** Focused-ion beam scanning electron microscopy (FIBSEM) was performed on a HeLa cell expressing Y192C ATL3-GFP. This video shows a perinuclear region of this cell (Fig. 5 and Video 6). 3D reconstruction of the ER reveals extensive lateral tubule tethering (Fig. 5). Different colors indicate tubules that are not continuous within the reconstructed volume.

		Monomeric Species			*Dimeric Species*			*Total*
Condition	***ATL3***	***Mw (kDa)***	***Calculated mass (µg)***	***Mass fraction (%)***	***Mw (kDa)***	***Calculated mass (µg)***	***Mass fraction (%)***	***Calculated mass (µg)***
Mg^{2+}	***WT***	47.3 ± 0.4	72.36	80.40	n/d	n/d	n/d	90.04
	Y192C	47.6 ± 0.2	90.30	90.90	n/d	n/d	n/d	99.38
	P338R	49.5 ± 0.2	74.34	92.00	n/d	n/d	n/d	80.82
Mg^{2+} GDP	***WT***	50.7 ± 0.6	67.46	94.80	n/d	n/d	n/d	71.13
	Y192C	49.2 ± 0.2	72.70	89.20	n/d	n/d	n/d	81.48
	P338R	49.3 ± 0.5	68.31	83.60	n/d	n/d	n/d	81.71
Mg^{2+} GTP-γ-S	***WT***	51.3 ± 0.2	39.13	51.80	92 ± 3	32.50	43.00	75.54
	Y192C	48.4 ± 0.4	71.39	75.00	80 ± 8	21.13	22.20	95.21
	P338R	53.3 ± 0.3	56.25	75.60	100 ± 10	16.47	22.20	74.35
Mg^{2+} GDP.AlF^4	***WT***	60 ± 1	12.14	20.40	102 ± 1	39.80	66.90	59.51
	Y192C	54.3 ± 0.8	35.60	47.10	96.6 ± 0.7	32.26	42.70	75.51
	P338R	58.3 ± 0.8	22.13	29.70	92 ± 2	38.68	51.90	74.50

Table S1: **Molecular weights and mass fractions of ATL3 WT, Y192C and P338R SEC-MALLS peaks.** Molecular weights displayed are the average MW, as determined with light scattering and differential light scattering data in the ASTRA software package (Wyatt) over a window of 0.9 minutes around the middle of the corresponding peak. Calculated masses represents the total mass of protein within the total peak based on differential refractive index data (dn/dc = 0.1820 ml/g).

REFERENCES

Arganda-Carreras, I., R. Fernandez-Gonzalez, A. Munoz-Barrutia, and C. Ortiz-De-Solorzano. 2010. 3D reconstruction of histological sections: Application to mammary gland tissue. *Microsc Res Tech*. 73:1019-1029.

Bian, X., R.W. Klemm, T.Y. Liu, M. Zhang, S. Sun, X. Sui, X. Liu, T.A. Rapoport, and J. Hu. 2011. Structures of the atlastin GTPase provide insight into homotypic fusion of endoplasmic reticulum membranes. *Proceedings of the National Academy of Sciences of the United States of America*. 108:3976-3981.

Böhm. 1997. CDNN.

Byrnes, L., and H. Sondermann. 2011. Structural basis for the nucleotide-dependent dimerization of the large G protein atlastin-1/SPG3A. *PNAS*.

Byrnes, L.J., A. Singh, K. Szeto, N.M. Benvin, J.P. O'Donnell, W.R. Zipfel, and H. Sondermann. 2013. Structural basis for conformational switching and GTP loading of the large G protein atlastin. *The EMBO journal*. 32:369-384.

de Bot, S.T., J.H. Veldink, S. Vermeer, A.R. Mensenkamp, F. Brugman, H. Scheffer, L.H. van den Berg, H.P. Kremer, E.J. Kamsteeg, and B.P. van de Warrenburg. 2013. ATL1 and REEP1 mutations in hereditary and sporadic upper motor neuron syndromes. *J Neurol*. 260:869-875.

English, A.R., and G.K. Voeltz. 2013. Endoplasmic reticulum structure and interconnections with other organelles. *Cold Spring Harb Perspect Biol*. 5:a013227.

Fischer, D., M. Schabhuttl, T. Wieland, R. Windhager, T.M. Strom, and M. Auer-Grumbach. 2014. A novel missense mutation confirms ATL3 as a gene for hereditary sensory neuropathy type 1. *Brain*. 137.

Greenfield, N.J. 2006. Using circular dichroism spectra to estimate protein secondary structure. *Nature protocols*. 1:2876-2890.

Guelly, C., P.-P.P. Zhu, L. Leonardis, L. Papić, J. Zidar, M. Schabhüttl, H. Strohmaier, J. Weis, T.M. Strom, J. Baets, J. Willems, P. De Jonghe, M.M. Reilly, E. Fröhlich, M. Hatz, S. Trajanoski, T.R. Pieber, A.R. Janecke, C. Blackstone, and M. Auer-Grumbach. 2011. Targeted high-throughput sequencing identifies mutations in atlastin-1 as a cause of hereditary sensory neuropathy type I. *American journal of human genetics*. 88:99-105.

Hu, J., and T.A. Rapoport. 2016. Fusion of the endoplasmic reticulum by membrane-bound GTPases. *Seminars in Cell & Developmental Biology*.

Hu, J., Y. Shibata, P.-P.P. Zhu, C. Voss, N. Rismanchi, W.A. Prinz, T.A. Rapoport, and C. Blackstone. 2009. A class of dynamin-like GTPases involved in the generation of the tubular ER network. *Cell*. 138:549-561.

Hu, X., F. Wu, S. Sun, W. Yu, and J. Hu. 2015. Human atlastin GTPases mediate differentiated fusion of endoplasmic reticulum membranes. *Protein & cell*. 6:307-311.

Hübner, C.A., and I. Kurth. 2014. Membrane-shaping disorders: a common pathway in axon degeneration. *Brain : a journal of neurology*. 137:3109-3121.

Jones, V.C., J.J.J. Rodríguez, A. Verkhratsky, and O.T. Jones. 2009. A lentivirally delivered photoactivatable GFP to assess continuity in the endoplasmic reticulum of neurones and glia. *Pflugers Archiv : European journal of physiology*. 458:809-818.

Kamentsky, L., T.R. Jones, A. Fraser, M.A. Bray, D.J. Logan, K.L. Madden, V. Ljosa, C. Rueden, K.W. Eliceiri, and A.E. Carpenter. 2011. Improved structure, function and compatibility for CellProfiler: modular high-throughput image analysis software. *Bioinformatics*. 27:1179-1180.

Knott, G., S. Rosset, and M. Cantoni. 2011. Focussed ion beam milling and scanning electron microscopy of brain tissue. *J Vis Exp*:e2588.

Kornak, U., I. Mademan, M. Schinke, M. Voigt, P. Krawitz, J. Hecht, F. Barvencik, T. Schinke, S. Gießelmann, F.T. Beil, A. Pou-Serradell, J.J. Vílchez, C. Beetz, T. Deconinck, V. Timmerman, C.

Kaether, P. De Jonghe, C.A. Hübner, A. Gal, M. Amling, S. Mundlos, J. Baets, and I. Kurth. 2014. Sensory neuropathy with bone destruction due to a mutation in the membrane-shaping atlastin GTPase 3. *Brain : a journal of neurology*. 137:683-692.

Kredel, S., F. Oswald, K. Nienhaus, K. Deuschle, C. Röcker, M. Wolff, R. Heilker, G.U. Nienhaus, and J. Wiedenmann. 2009. mRuby, a bright monomeric red fluorescent protein for labeling of subcellular structures. *PloS one*. 4.

Kremer, A., S. Lippens, S. Bartunkova, B. Asselbergh, C. Blanpain, M. Fendrych, A. Goossens, M. Holt, S. Janssens, M. Krols, J.C. Larsimont, C. Mc Guire, M.K. Nowack, X. Saelens, A. Schertel, B. Schepens, M. Slezak, V. Timmerman, C. Theunis, V.A.N.B. R, Y. Visser, and C.J. Guerin. 2015. Developing 3D SEM in a broad biological context. *Journal of microscopy*. 259:80-96.

Larkin, M.A., G. Blackshields, N.P. Brown, R. Chenna, P.A. McGettigan, H. McWilliam, F. Valentin, I.M. Wallace, A. Wilm, R. Lopez, J.D. Thompson, T.J. Gibson, and D.G. Higgins. 2007. Clustal W and Clustal X version 2.0. *Bioinformatics (Oxford, England)*. 23:2947-2948.

Liu, T.Y., X. Bian, F.B. Romano, T. Shemesh, T.A. Rapoport, and J. Hu. 2015. Cis and trans interactions between atlastin molecules during membrane fusion. *Proceedings of the National Academy of Sciences of the United States of America*. 112:60.

Liu, T.Y., X. Bian, S. Sun, X. Hu, R.W. Klemm, W.A. Prinz, T.A. Rapoport, and J. Hu. 2012. Lipid interaction of the C terminus and association of the transmembrane segments facilitate atlastin-mediated homotypic endoplasmic reticulum fusion. *Proceedings of the National Academy of Sciences of the United States of America*. 109:54.

McCorquodale, D.S., 3rd, U. Ozomaro, J. Huang, G. Montenegro, A. Kushman, L. Citrigno, J. Price, F. Speziani, M.A. Pericak-Vance, and S. Zuchner. 2011. Mutation screening of spastin, atlastin, and REEP1 in hereditary spastic paraplegia. *Clin Genet*. 79:523-530.

Morin-Leisk, J., S.G. Saini, X. Meng, A.M. Makhov, P. Zhang, and T.H. Lee. 2011. An intramolecular salt bridge drives the soluble domain of GTP-bound atlastin into the postfusion conformation. *J Cell Biol*. 195:605-615.

Moss, T.J., C. Andreazza, A. Verma, A. Daga, and J.A. McNew. 2011. Membrane fusion by the GTPase atlastin requires a conserved C-terminal cytoplasmic tail and dimerization through the middle domain. *Proceedings of the National Academy of Sciences of the United States of America*. 108:11133-11138.

Namekawa, M., M.P.P. Muriel, A. Janer, M. Latouche, A. Dauphin, T. Debeir, E. Martin, C. Duyckaerts, A. Prigent, C. Depienne, A. Sittler, A. Brice, and M. Ruberg. 2007. Mutations in the SPG3A gene encoding the GTPase atlastin interfere with vesicle trafficking in the ER/Golgi interface and Golgi morphogenesis. *Molecular and cellular neurosciences*. 35:1-13.

O'Donnell, J.P., R.B. Cooley, C.M. Kelly, K. Miller, O.S. Andersen, R. Rusinova, and H. Sondermann. 2017. Timing and Reset Mechanism of GTP Hydrolysis-Driven Conformational Changes of Atlastin. *Structure*. 25:997-1010 e1014.

Orso, G., D. Pendin, S. Liu, J. Tosetto, T.J. Moss, J.E. Faust, M. Micaroni, A. Egorova, A. Martinuzzi, and J.A. McNew. 2009. Homotypic fusion of ER membranes requires the dynamin-like GTPase atlastin. *Nature*. 460:978-983.

Pettersen, E.F., T.D. Goddard, C.C. Huang, G.S. Couch, D.M. Greenblatt, E.C. Meng, and T.E. Ferrin. 2004. UCSF Chimera?A visualization system for exploratory research and analysis. *Journal of Computational Chemistry*. 25:1605-1612.

Rismanchi, N., C. Soderblom, J. Stadler, P.P. Zhu, and C. Blackstone. 2008. Atlastin GTPases are required for Golgi apparatus and ER morphogenesis. *Hum Mol Genet*. 17:1591-1604.

Saini, S.G., C. Liu, P. Zhang, and T.H. Lee. 2014. Membrane tethering by the atlastin GTPase depends on GTP hydrolysis but not on forming the cross-over configuration. *Molecular biology of the cell*. 25:3942-3953.

Salmon, P., and D. Trono. 2006. Production and titration of lentiviral vectors. *Curr Protoc Neurosci*. Chapter 4:Unit 4 21.

Schindelin, J., I. Arganda-Carreras, E. Frise, V. Kaynig, M. Longair, T. Pietzsch, S. Preibisch, C. Rueden, S. Saalfeld, B. Schmid, J.Y. Tinevez, D.J. White, V. Hartenstein, K. Eliceiri, P. Tomancak, and A.

Cardona. 2012. Fiji: an open-source platform for biological-image analysis. *Nat Methods*. 9:676-682.

Schneider, C.A., W.S. Rasband, and K.W. Eliceiri. 2012. NIH Image to ImageJ: 25 years of image analysis. *Nat Methods*. 9:671-675.

Schrödinger, L. 2015. The {PyMOL} Molecular Graphics System, Version~1.8.

Ulengin, I., J.J. Park, and T.H. Lee. 2015. ER network formation and membrane fusion by atlastin1/SPG3A disease variants. *Mol Biol Cell*. 26:1616-1628.

Webb, B., and A. Sali. 2016. Comparative Protein Structure Modeling Using MODELLER. *In* Current Protocols in Protein Science. Vol. 86. John Wiley & Sons, Inc., Hoboken, NJ, USA. 2.9.1-2.9.37.

Westrate, L.M., J.E. Lee, W.A. Prinz, and G.K. Voeltz. 2015. Form follows function: the importance of endoplasmic reticulum shape. *Annual review of biochemistry*. 84:791-811.

Winsor, J., D.D. Hackney, and T.H. Lee. 2017. The crossover conformational shift of the GTPase atlastin provides the energy driving ER fusion. *J Cell Biol*.

Zhao, X., D. Alvarado, S. Rainier, R. Lemons, P. Hedera, C.H. Weber, T. Tukel, M. Apak, T. Heiman-Patterson, L. Ming, M. Bui, and J.K. Fink. 2001. Mutations in a newly identified GTPase gene cause autosomal dominant hereditary spastic paraplegia. *Nat Genet*. 29:326-331.

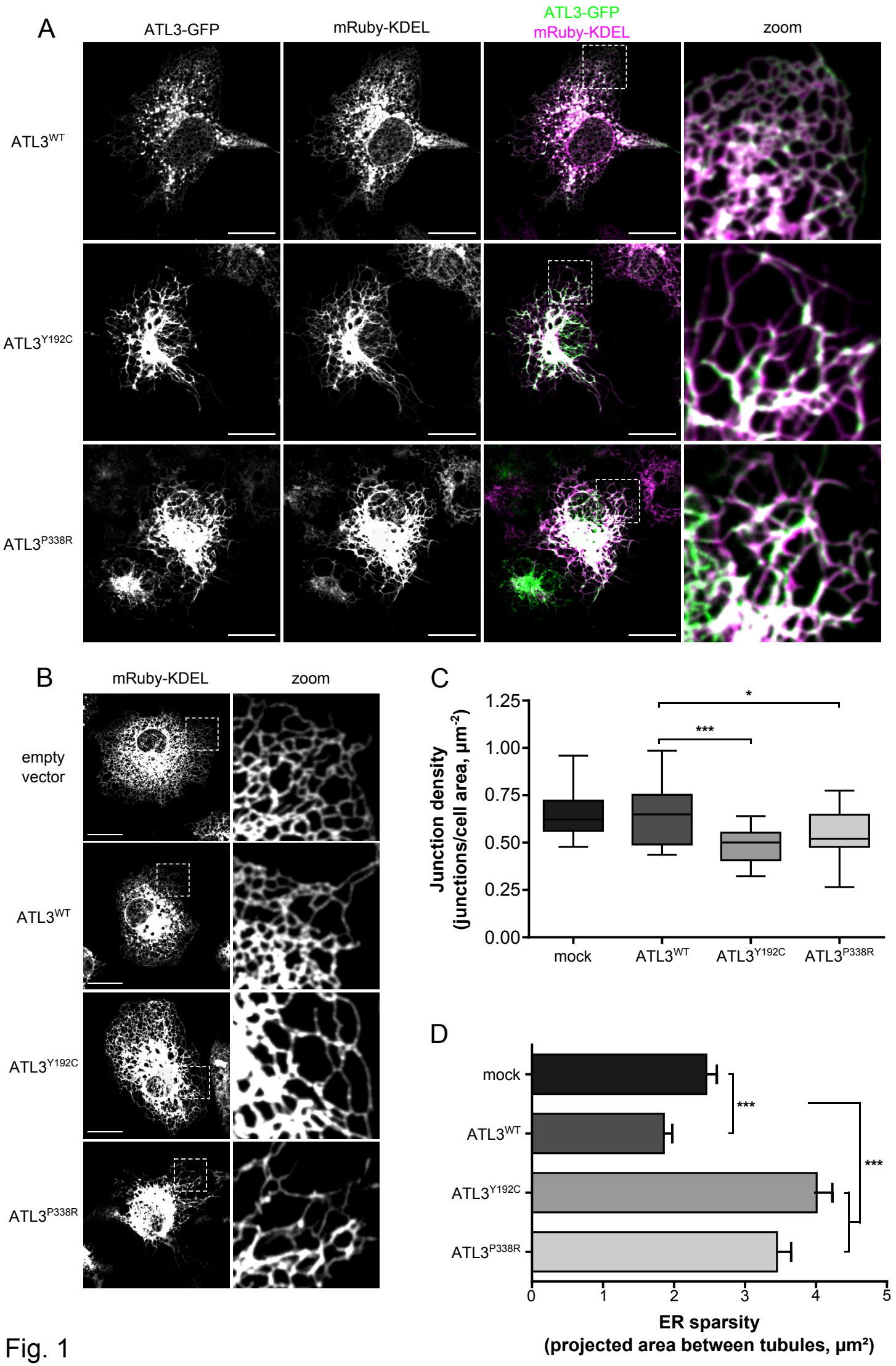
A
ATL3-GFP
mRuby-KDEL
ATL3-GFP
mRuby-KDEL
zoom
ATL3WT
ATL3Y192C
ATL3P338R
B
mRuby-KDEL
zoom
empty vector
ATL3WT
ATL3Y192C
ATL3P338R
C
Junction density (junctions/cell area, µm-2)
1.25
1.00
0.75
0.50
0.25
0.00
*
***
mock
ATL3WT
ATL3Y192C
ATL3P338R
D
mock
ATL3WT
ATL3Y192C
ATL3P338R
***
***
0
1
2
3
4
5
ER sparsity
(projected area between tubules, µm²)

Fig. 1

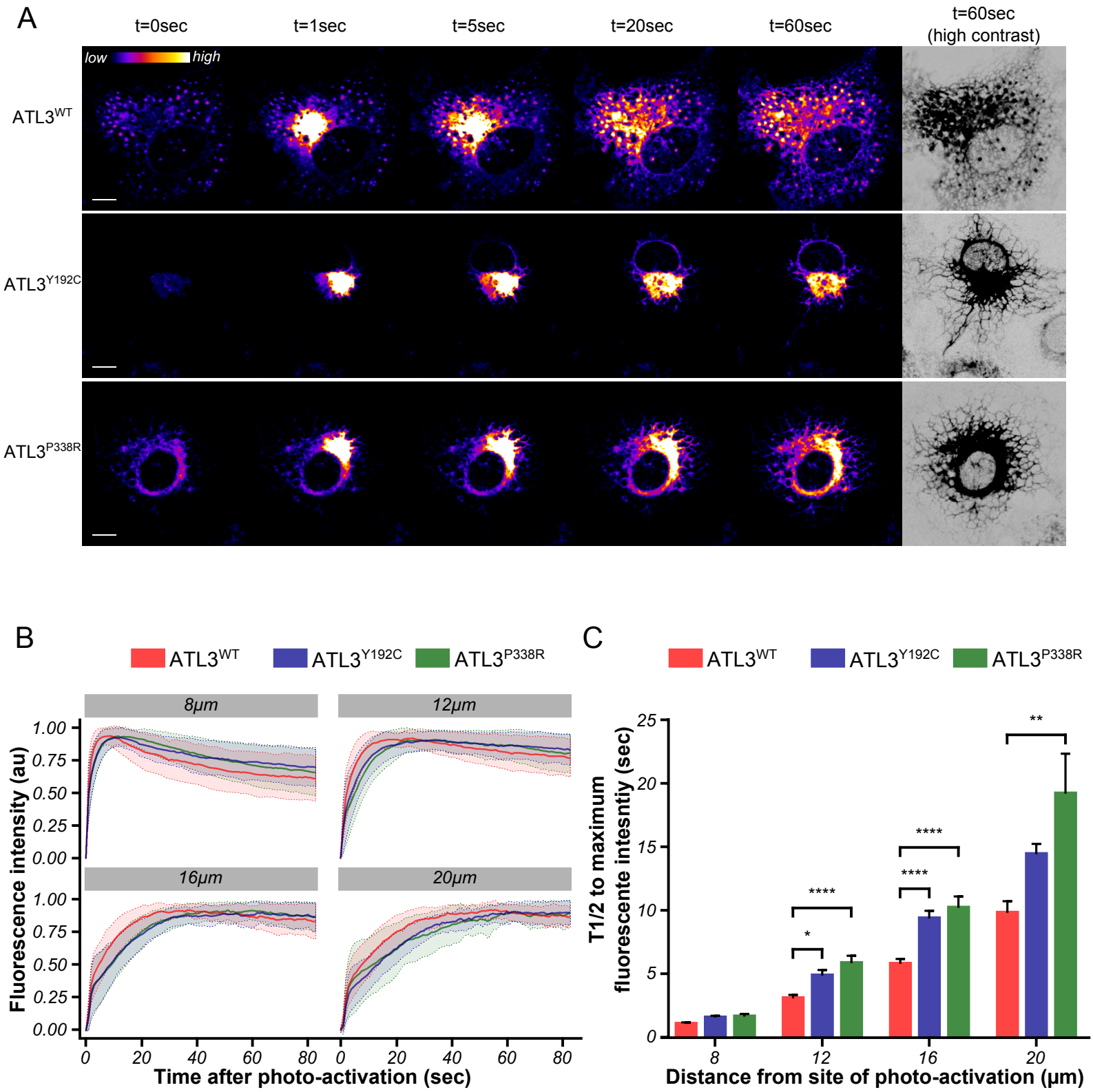
A
t=0sec
t=1sec
t=5sec
t=20sec
t=60sec
t=60sec
(high contrast)
low
high
ATL3WT
ATL3Y192C
ATL3P338R
B
ATL3WT
ATL3Y192C
ATL3P338R
8μm
12μm
16μm
20μm
Fluorescence intensity (au)
1.00
0.75
0.50
0.25
0.00
0
20
40
60
80
Time after photo-activation (sec)
C
ATL3WT
ATL3Y192C
ATL3P338R
T1/2 to maximum
fluorescente intesntiy (sec)
25
20
15
10
5
0
*
****
****
****
**
8
12
16
20
Distance from site of photo-activation (μm)

Fig. 2

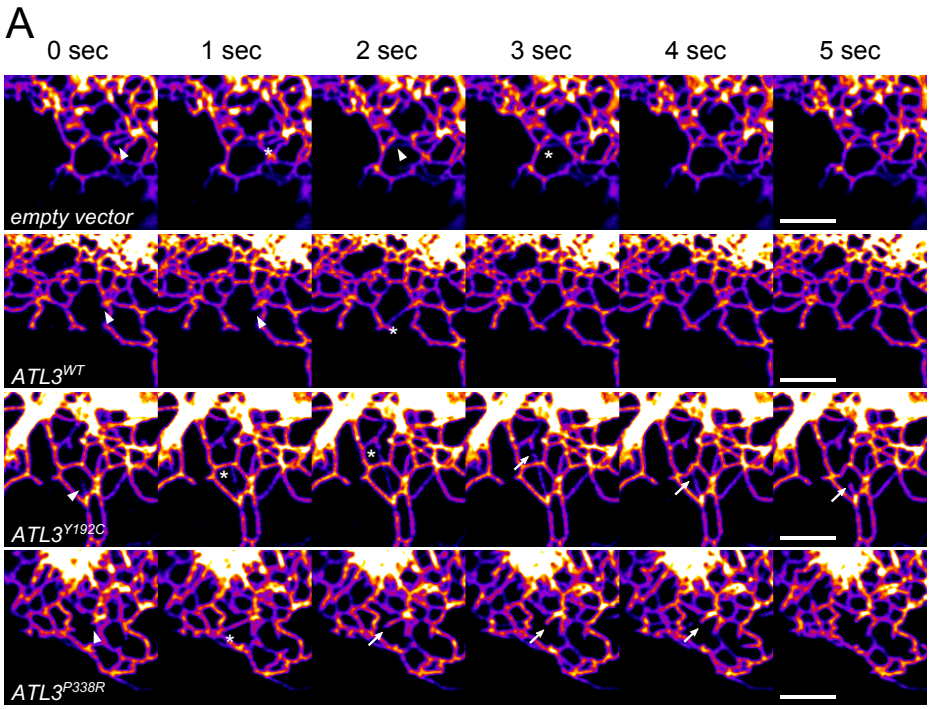
A
0 sec
1 sec
2 sec
3 sec
4 sec
5 sec
empty vector
ATL3WT
ATL3Y192C
ATL3P338R

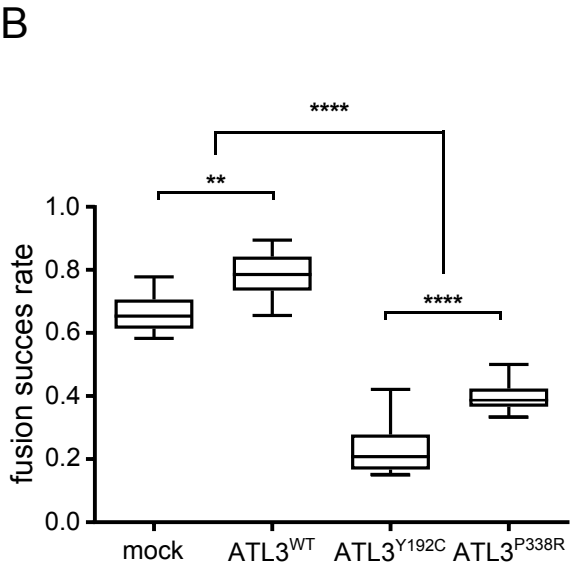
B
fusion succes rate
1.0
0.8
0.6
0.4
0.2
0.0
**
****
****
mock
ATL3WT
ATL3Y192C
ATL3P338R

Fig. 3

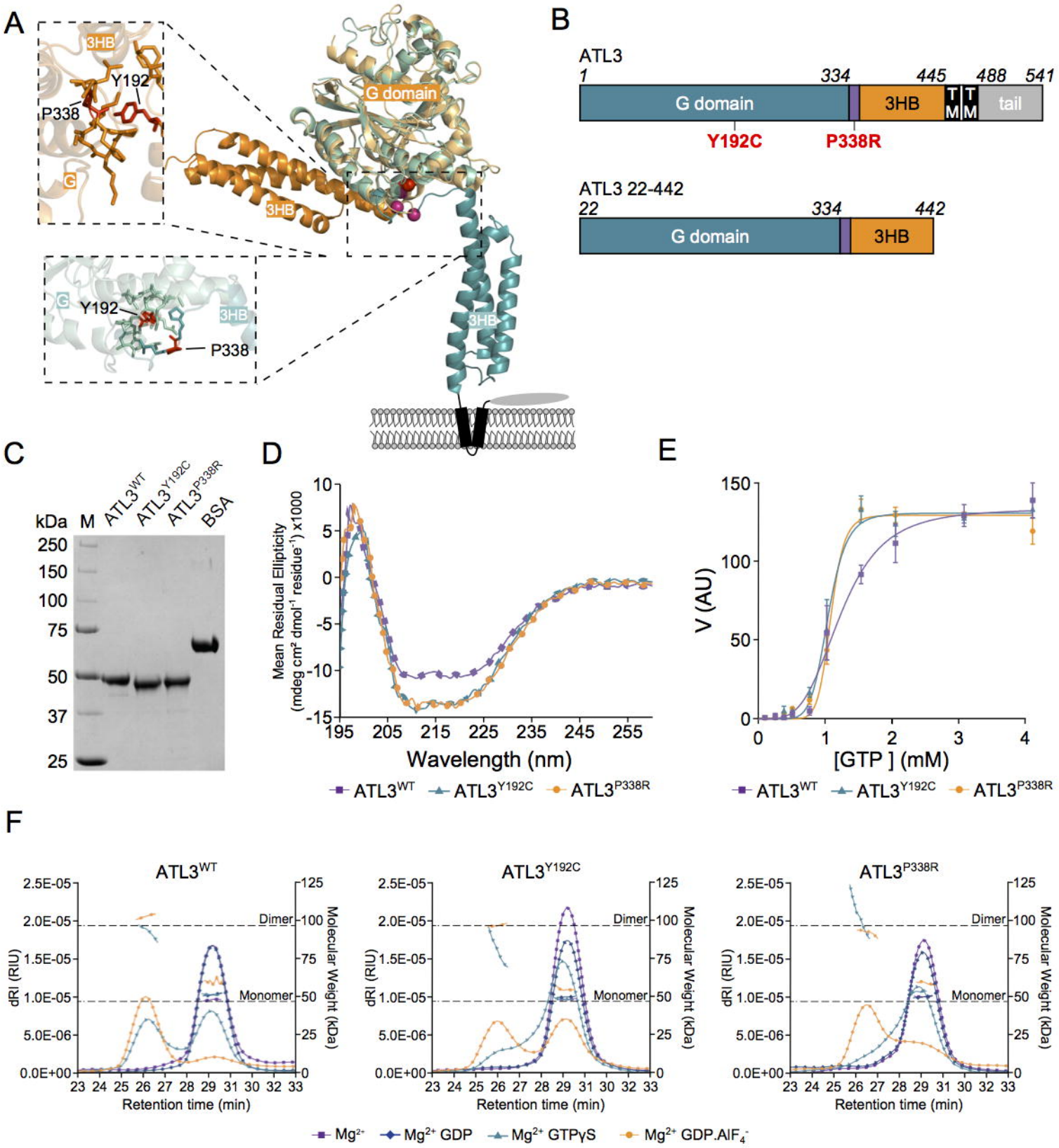
A
3HB
Y192
P338
G
G domain
3HB
G
Y192
3HB
P338
3HB
B
ATL3
1
334
445
488
541
G domain
3HB
TM
TM
tail
Y192C
P338R
ATL3 22-442
22
334
442
G domain
3HB
C
kDa
M
ATL3WT
ATL3Y192C
ATL3P338R
BSA
250
150
100
75
50
37
25
D
Mean Residual Ellipticity (mdeg cm² dmol⁻¹ residue⁻¹) x1000
Wavelength (nm)
ATL3WT
ATL3Y192C
ATL3P338R
E
V (AU)
[GTP] (mM)
ATL3WT
ATL3Y192C
ATL3P338R
F
ATL3WT
ATL3Y192C
ATL3P338R
dRI (RIU)
Molecular Weight (kDa)
Dimer
Monomer
Retention time (min)
Mg2+
Mg2+ GDP
Mg2+ GTPγS
Mg2+ GDP.AlF4-

Fig. 4

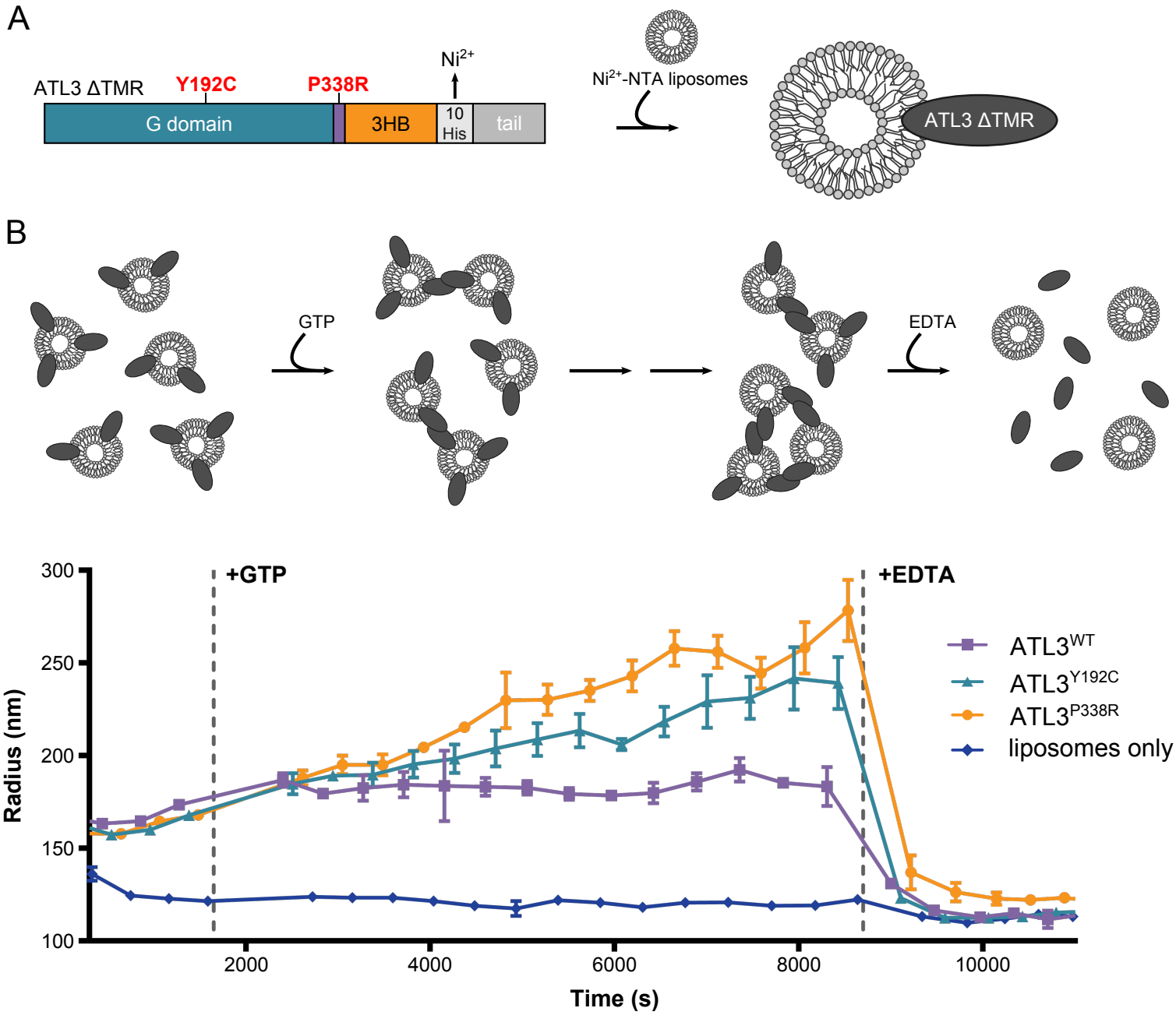
A
ATL3 ΔTMR
Y192C
P338R
Ni2+
G domain
3HB
10 His
tail
Ni2+-NTA liposomes
ATL3 ΔTMR
B
GTP
EDTA
+GTP
+EDTA
Radius (nm)
Time (s)
300
250
200
150
100
2000
4000
6000
8000
10000
ATL3WT
ATL3Y192C
ATL3P338R
liposomes only

Fig. 5

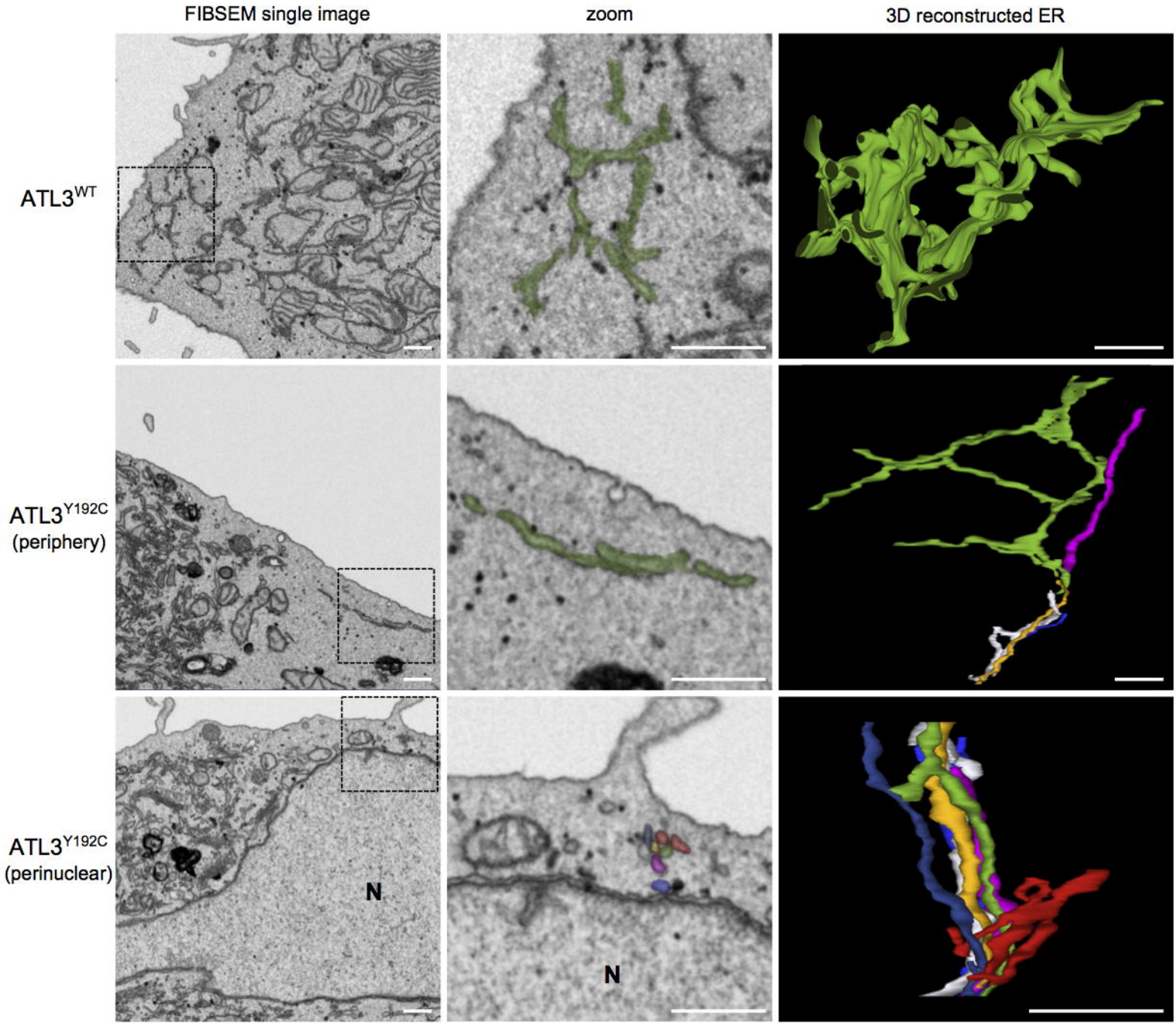
FIBSEM single image
zoom
3D reconstructed ER
ATL3WT
ATL3Y192C
(periphery)
ATL3Y192C
(perinuclear)
N
N

Fig. 6

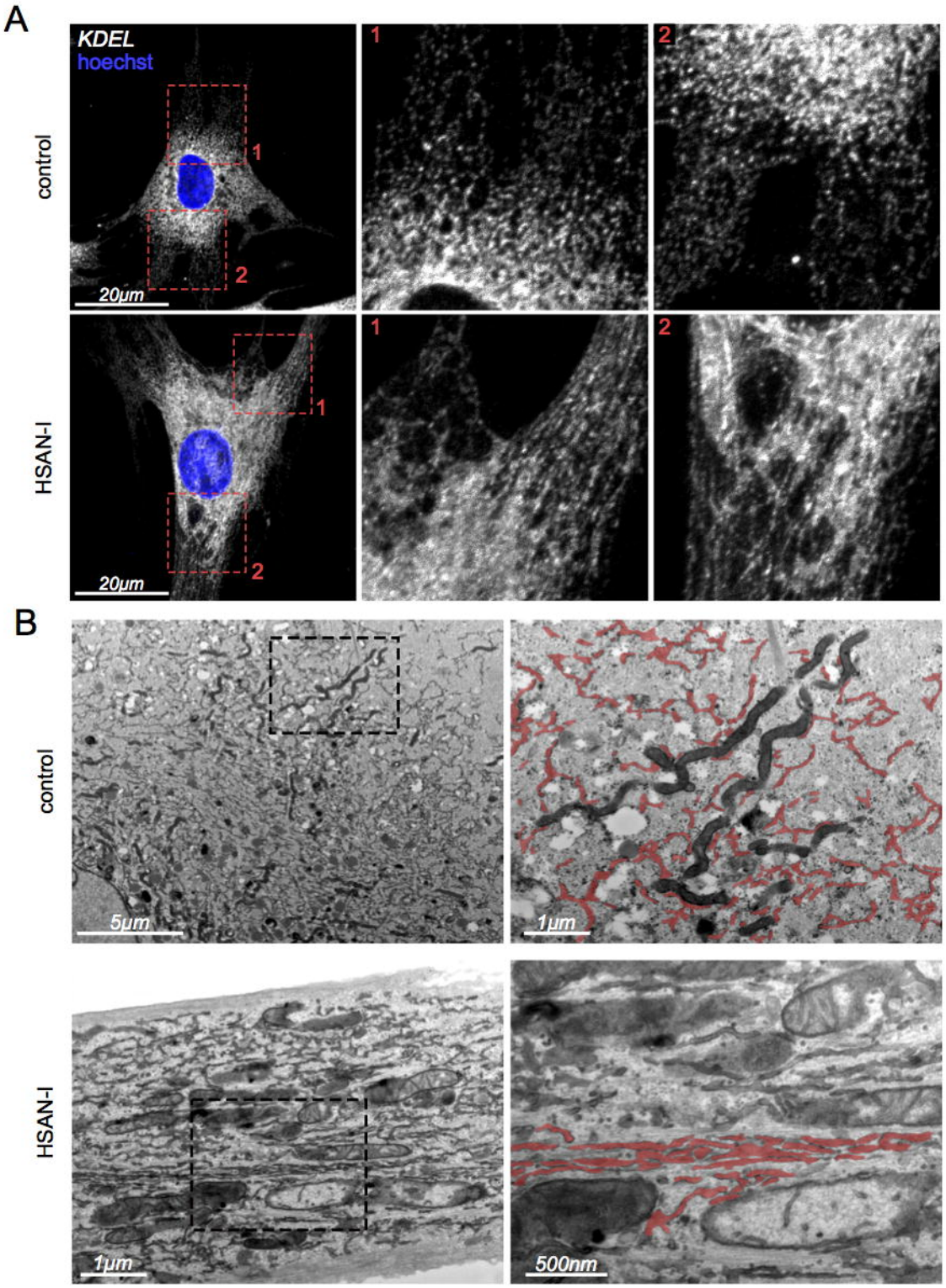

Fig. 7

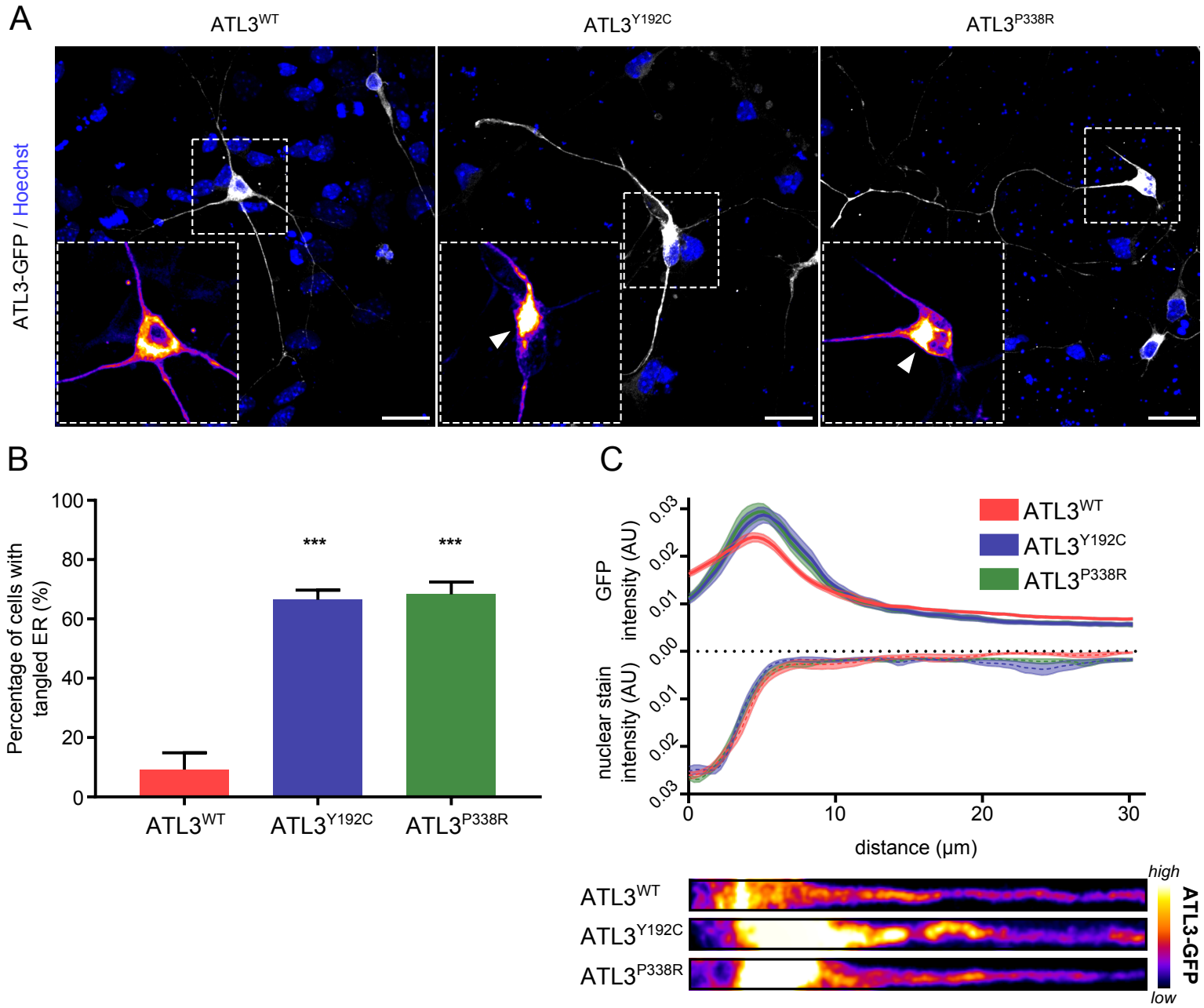
A
ATL3WT
ATL3Y192C
ATL3P338R
ATL3-GFP / Hoechst
B
Percentage of cells with tangled ER (%)
100
80
60
40
20
0
***
***
ATL3WT
ATL3Y192C
ATL3P338R
C
GFP intensity (AU)
nuclear stain intensity (AU)
0.03
0.02
0.01
0.00
0.01
0.02
0.03
0
10
20
30
distance (μm)
ATL3WT
ATL3Y192C
ATL3P338R
high
low
ATL3-GFP

Fig. 8

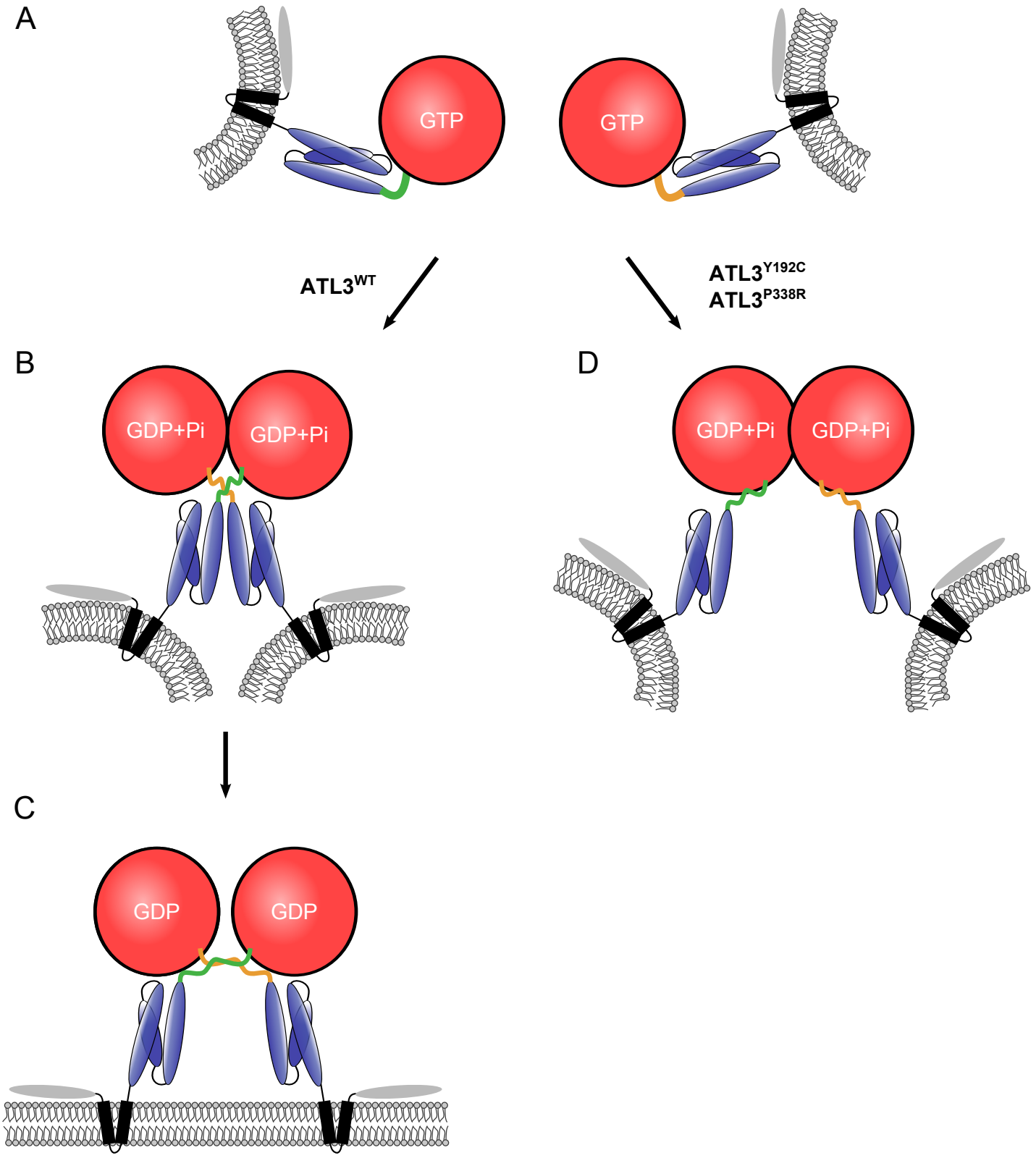
A
GTP
GTP
ATL3WT
ATL3Y192C
ATL3P338R
B
GDP+Pi
GDP+Pi
D
GDP+Pi
GDP+Pi
C
GDP
GDP

Fig. 9